



## Extracting energy from ocean thermal and salinity gradients to power unmanned underwater vehicles: State of the art, current limitations, and future outlook

Hyunjun Jung<sup>a</sup>, Chinmayee V. Subban<sup>a</sup>, Joshua Dominic McTigue<sup>b</sup>, Jayson J. Martinez<sup>a</sup>, Andrea E. Copping<sup>a</sup>, Julian Osorio<sup>c</sup>, Jian Liu<sup>a</sup>, Z. Daniel Deng<sup>a,\*</sup>

<sup>a</sup> Energy and Environment Directorate, Pacific Northwest National Laboratory, Richland, WA 99354, USA

<sup>b</sup> National Renewable Energy Laboratory, Golden, CO 80401, USA

<sup>c</sup> Center for Energy Conversion & Storage Systems, National Renewable Energy Laboratory, Golden, CO 80401, United States

### ARTICLE INFO

#### Keywords:

Thermal gradient  
Salinity gradient  
Unmanned underwater vehicle  
Energy harvesting  
Phase change material

### ABSTRACT

Thermal gradient energy-generation technologies for powering unmanned underwater vehicles (UUVs) or autonomous sensing systems in the ocean are mainly in the research development phase or commercially available at a limited scale, and salinity-gradient energy-generation technologies have not been adequately researched yet. The demand for self-powered UUVs suitable for long-term deployments has been growing, and further research related to small-scale ocean gradient energy systems is needed. In this study, we conducted a comprehensive review about harvesting energy from ocean thermal or salinity gradients for powering UUVs, focusing on gliders and profiling floats. Thermal gradient energy systems for UUVs based on phase change materials (PCM) cannot provide the energy required for powering autonomous sensing systems because of the systems' low energy conversion efficiency. Besides reducing energy consumption by developing more efficient electrical-mechanical systems, enhancing the thermal conductivity of the PCMs may help address this challenge by increasing the power generation rate of the UUVs. Several other emerging technologies, such as thermoelectric generators, shape memory alloys, and small-scale thermodynamic cycle systems, have shown potential for powering UUVs, but they are still only at the laboratory testing or conceptual design phase. The most advanced power generation technologies based on salinity gradients, reverse electrodialysis and pressure-retarded osmosis, are still not economically viable for large-scale deployment, mainly because of the high cost of the components required to operate in harsh saline environments. Our feasibility evaluation showed that existing salinity gradient power generation technologies are not directly feasible for powering UUVs in the open ocean.

### 1. Introduction

There is increasing demand for unmanned underwater vehicles (UUVs) that are capable of long duration deployments (e.g., several years) for ocean observation [1–4]. Gliders and profiling floats are two examples of UUVs that use changes in buoyancy to drive vertical propulsion. The key difference between these two UUVs is the rate at which they ascend/descend. Gliders have hydrofoils, or underwater wings, which allow them to exploit the vertical motion resulting from the buoyancy change to glide in the forward direction (Fig. 1) [5]. A profiling float uses the buoyancy change to merely alter the depth of the

UUV and is otherwise simply drifting with the ocean currents (Fig. 2) [6]. A profiling float spends most of its time passively drifting with the ocean currents at a specific depth.

The service life of gliders and profiling floats is critically important for sustainable and reliable ocean observation. However, the average service life of float-type UUVs is only approximately 135 vertical profiling cycles, which necessitates limiting vertical profiles to a typical rate of once every 9 days to obtain a typical service life of between 3 and 5 years [7]. This limited service life results in increased environmental monitoring program costs because the floats typically fail at depth necessitating replacement at a cost of more than \$20K [2,8]. Even if the

\* Corresponding author.

E-mail address: [Zhiqun.deng@pnnl.gov](mailto:Zhiqun.deng@pnnl.gov) (Z.D. Deng).

floats can be serviced, the ship and crew time can still result in costs ranging from \$3K to \$15K per servicing and present risk to human life [1,2]. If the service life could be increased, not only would program costs decrease but it would allow for more demanding applications; for example, in the case of vertically profiling floats there is a need to profile to deeper depths and to increase the sensing capabilities, for instance, by adding biogeochemical sensing capabilities [2].

Ocean gradient energy is a promising solution to extending the service life of UUVs. Since 1995, thermal gradient energy has been researched for powering UUVs [9], and phase change material (PCM)-based UUVs are commercially available at a limited scale. However, the energy requirement for powering autonomous sensing systems in UUVs has been increasing over time because of increasing sensing needs [9]. Powering UUVs using naturally occurring salinity gradients (between the surface and subsea) would offer new ways of extracting marine renewable energy. While extensive research on salinity-gradient energy in coastal areas has been conducted, the feasibility of using small salinity gradients to power UUVs in the open ocean away from mouths of rivers has not been sufficiently explored to date.

To evaluate the feasibility of using ocean gradients to increase the service life of UUVs, we conducted a comprehensive review of the literature about generating power from thermal or salinity gradients. In this paper, we describe relevant technologies and document their current status and limitations. In addition, we present a preliminary evaluation of the energy output for the most advanced of these technologies for powering UUVs in low-salinity gradients.

## 2. Energy use

The total energy use per profile of float and glide-type UUVs varies from 1.1 to 14.7 Wh, depending on the diving depth, speed, and total weight of the UUV. The total energy consumption of the glider-type UUVs ranges between 1.5 and 14.7 Wh, which is higher than the energy used by the float-type UUVs (1.1–7.4 Wh), because of their heavy weight and fast diving speed. Table 1 shows the energy use of the components of selected float and glider-type UUVs with their diving

depths, speeds, and total weights. A fast diving speed requires a large volume change in the UUV, thus the buoyancy engine would require high power [10]. The diving speed and total weight of the float-type UUVs are 8–10 cm/s and 18–45 kg, respectively [3,4,11–13]. In the case of the glider-type UUVs, the diving speed and total weight are 24–38 cm/s and 52–65 kg, which are 2–4 times and 2–3 times higher than the float-type UUVs, respectively [8,10,14,15]. The glider-type UUVs also require a pitch regulation motor for attitude regulation. For example, the pitch regulation motor of the Petrel-II glider achieves attitude regulation by moving a battery pack along the glider's central axis [10]. The power consumption of the pitch regulation motor is 4W [10], which greatly affects the energy consumption of the glider-type UUVs. Nevertheless, glider-type UUVs moving at low speeds, consume less energy. Recently, Bruvik et al. described the low-power Seaglider that dives with slow speed (5 cm/s) and minimum volume change [2]. This glider used 1.5 Wh of energy per profile. The number of sensors, and the power consumption of the different sensors onboard the UUV also affect its total energy requirements. The reported energy use per profile of the University of Washington-Built SOCCOM Apex float (5.5 Wh) is almost two times higher than that of the SOLO II [3,4], largely due to the 2.2 Wh sensors' power consumption. The period of activity of the sensors also affects the total energy requirement of the UUVs. In fact, Hockley reported that for the Seaglider, when the sensors are activated for 100% of the profile time, the total energy use is 7.4 Wh [14]. This energy does not consider the effect of sensor scheduling (duty cycle). In the case of the Deep SOLO float [12], the conductivity, temperature, and pressure (CTD) sensors (SBE61, Sea-bird scientific) are operated in a mode to collect continuous profiles from the sea surface to a depth of 2000 m, but the sensors were used in discrete mode at 10 m intervals from 2000 m to the ocean bottom (6000 m). This strategy can result in a reduction of energy consumption of the sensors. The selection of the sensor model can also impact the total amount of energy used by a UUV. King et al. reported different combinations of sensors (Model: SBE CTD and RBR CTD) and buoyancy engine (Model: S2A and S2H) for the SOLO II float. Based on the combinations, the range of the total energy consumption of the SOLO II float is 1.1–2.9 Wh [4].

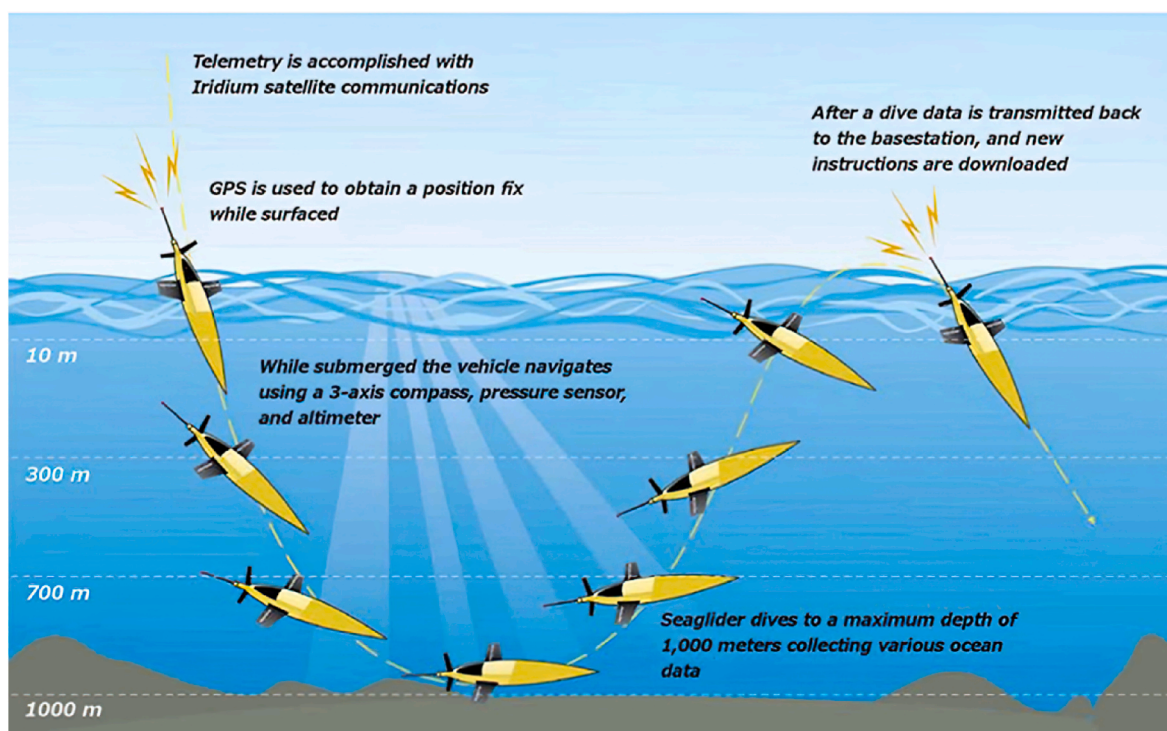


Fig. 1. Example of glider-type UUV motion during operation [5].

Of the total energy required by the UUVs, 28–78% is consumed by the buoyancy engine (Table 1). For example, for a deep dive (6000 m) of the Deep SOLO float, the buoyancy engine consumes 5.8 Wh, which accounts for 78% of the energy used [12]. As a result, this is the most energy-hungry component in float and glider-type UUVs, so reducing the energy consumed by the buoyancy engine is key to extending UUV mission durations. To effect a net change in buoyancy, a buoyancy engine within a UUV has internal and external bladders that are connected to an electric pump that transports hydraulic oil between them. The electric pump is the part that requires significant power. To reduce the power consumption of the electric pump, Asakawa et al. designed a bidirectionally functioning electric pump (Fig. 3a) that can draw oil from an external oil bladder in addition to pumping the oil into the bladder [16]. When the oil in the external bladder, under high pressure, flows into the oil reservoir the electric pump acts as an electric generator and the output power to a damping resistor is 30 W with 100 bars of hydraulic pressure.

Zhou et al. modeled the hybrid buoyancy regulating system (HBRS) to reduce the buoyancy engines energy consumption [17]. HBRS consists of an electric pump, external bladder, and an accumulator containing pre-charged compressed nitrogen gas (Fig. 3b). At the surface of the ocean, the valve between the external bladder and the accumulator opens, then the highly pressurized oil inside the external bladder compresses the nitrogen gas as it flows into the accumulator, thus accumulating energy. At depth in the ocean, the compressed nitrogen gas causes the hydraulic oil to flow back to the external bladder, which helps the electric pump increase the buoyancy. Simulation results of HBRS by Zhou et al. demonstrated that there can be a 30% reduction for the UUV overall energy requirement [17].

### 3. Thermal gradient energy

A brief description of thermal gradient-based energy-generation technologies is provided in this section and a summary of the state of the art is included in Table 4 (at the end of the section).

### 3.1. Phase change material-based UUVs

#### 3.1.1. Buoyancy regulation

PCM-based buoyancy regulation UUVs can use PCM as a thermal engine to store ocean thermal energy to later be converted to mechanical energy, thereby providing a power source for vertical propulsion during profiles. Fig. 4 shows the mechanism of the buoyancy regulation system in a UUV [18]. The accumulator is filled with pressurized oil when the UUV is at the surface, and the thermal material (PCM) maintains a liquid state at a temperature above the PCM's melting point (Fig. 4a). By opening solenoid valve A, the buoyancy of the glider is changed from positive to negative (Fig. 4b) and by transferring the oil from the external bladder to the internal one. As the UUV descends to deeper depths the water temperature decreases gradually. Once the threshold temperature where the PCM is converted from liquid to solid is passed, the PCM draws the oil to the thermal engine from the internal bladder (Fig. 4c). By opening solenoid valve B, oil is transferred from the accumulator to the external bladder and as a result the buoyancy of the glider is changed from negative to positive (Fig. 4d). The water temperature gradually increases as the UUV ascends toward the surface. Once the PCM's melting temperature is passed, as heat flows into the thermal engine the PCM pressurizes the oil causing it to fill the accumulator (Fig. 4a). The entire cycle repeats when harvesting the thermal gradient energy to produce the vertical force needed for gliding.

The total efficiency of a PCM-based buoyancy regulation type UUV was defined using two conversion steps: thermal-to-hydraulic energy conversion and hydraulic-to-kinetic energy. Wang et al. stated that the total efficiency of a PCM-based buoyancy regulation type UUV was about 0.29–0.33% (Table 4) [9]. Since 1995, several field tests of PCM-based buoyancy regulation type UUVs have been conducted [18–23]. The first deployment of a buoyancy regulation type UUV was performed in the Sargasso Sea in October 1995 by the Sea Education Association. Over a period of 240 days, the UUV performed 120 successful dive cycles before experiencing failure [19]. Yang et al. developed a thermal engine with a double-layer structure for a buoyancy regulation type UUV (Fig. 5) and increased the rate of volumetric change of the thermal engine by applying the isostatic pressing technology to improve its performance [18]. The authors deployed the prototype in the South China Sea in 2015 and reported that the actual rate of

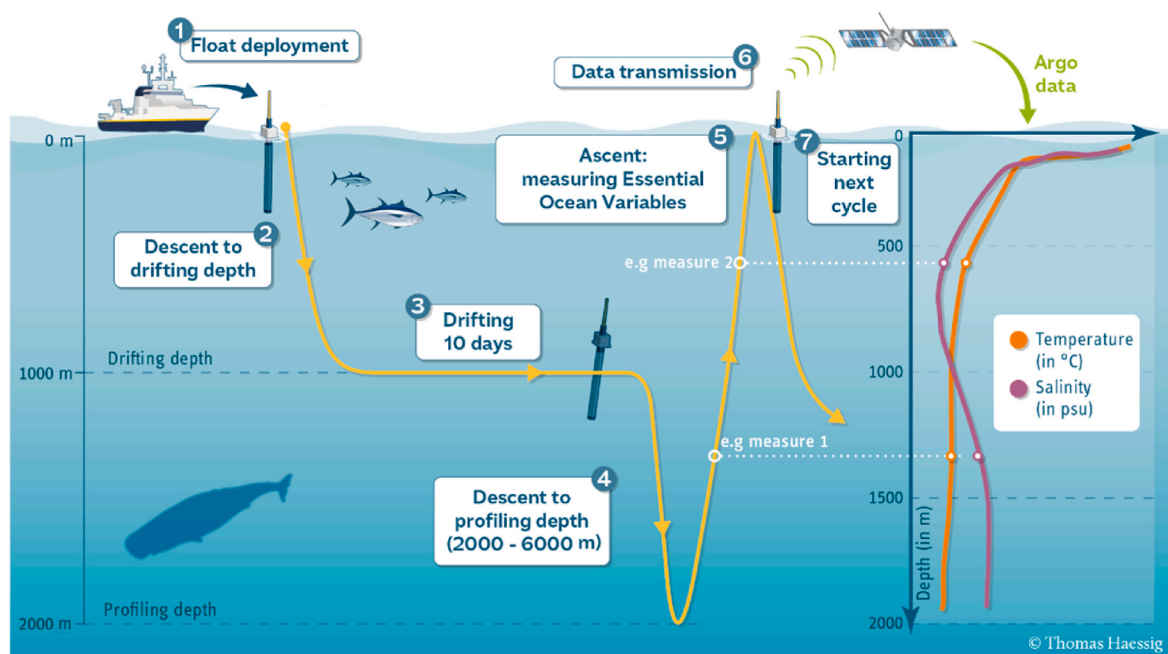
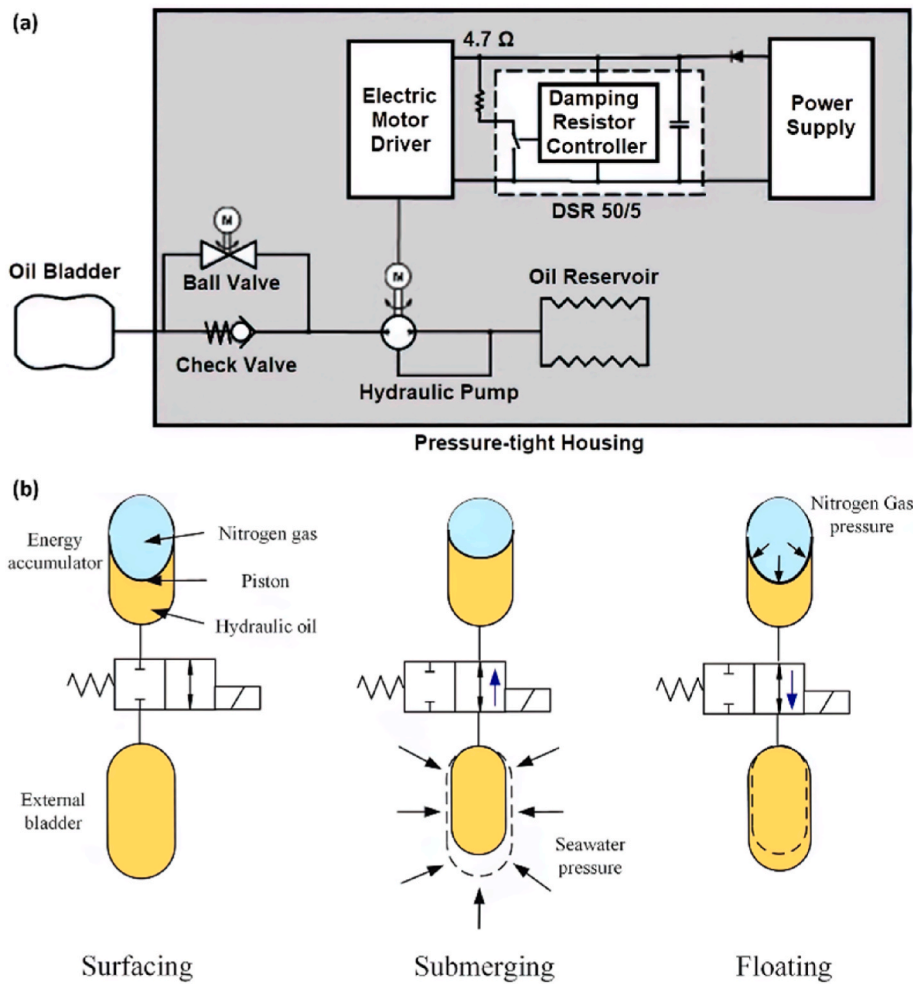


Fig. 2. Example of a profiling float-type UUV's motion during operation [6].

**Table 1**  
Energy use of UUVs and their component parts, per diving profile.

	SOCOM APEX Float	APEX Float (7553)	PROVOR Float (remOcean NKE CTS4)	SOLO II Float	Deep SOLO Float	Low-power Seaglider (sg564)	Seaglider	Petrel-II Glider	Solcom Glider
Depth (m)	2000	1050	2000		6000	1000	1000	200-1500	1000
Total Weight (kg)			40-45	18	27		52	68.9	52
Speed (cm/s)	8-10 (vertical)			9 (vertical)		5 (vertical) 8.5 (horizon)	34.9 (horizontal)	24-38	
Buoyancy Engine	6.42 kJ	4.01 kJ	10.25 kJ	3.0-5.5 kJ	21.1 kJ	1.633 kJ	9.96 kJ	Power: 28-55W	Power: 3-26 W
Attitude control						0.414 kJ		Power: 4W (Attitude: 45°)	Power: 2W
Controller	1.99 kJ	1.39 kJ	5.42 kJ	0.5 kJ		2.028 kJ		Power: 2W	
Satellite Communication	2.5 kJ	1.94	1.13 kJ		0.6 kJ	1.014 kJ		N/A	Power: 4.5 W
CTD sensor	3.04 kJ	2.8 kJ	4.56 kJ	0.5-4.5 kJ	5.2 kJ	0.321 kJ	16.9 kJ	Power: 0.2 W	Power: 0.1 W
Nitrate sensor	3.62 kJ	2.97 kJ	0.8 kJ						
Oxygen sensor	0.1 kJ	0.09 kJ	0.62 kJ						
FLBB sensor	0.16 kJ		2.13 kJ						
pH sensor	1.28 kJ								
Radiometry			0.22 kJ						
Altimeter								Power: 1.9W	
Battery Self-discharge	0.70 kJ	0.7 kJ	1.15 kJ						
Total energy use	19.8 kJ (5.5 Wh)	13.9 kJ (3.8 Wh)	26.3 kJ (7.3 Wh)	4.0-10.5 kJ (1.1-2.9 Wh)	26.9 kJ (7.4 Wh)	5.4 kJ (1.5 Wh)	26.8 kJ (7.5 Wh)	23.0-53.2 kJ (6.4-14.8 Wh)	
Reference	[3]	[11]	[13]	[4]	[12]	[2]	[14]	[10]	[15]



**Fig. 3.** Schematic of (a) bidirectionally functioning buoyancy engine [16] and (b) hybrid buoyancy regulating system [17].

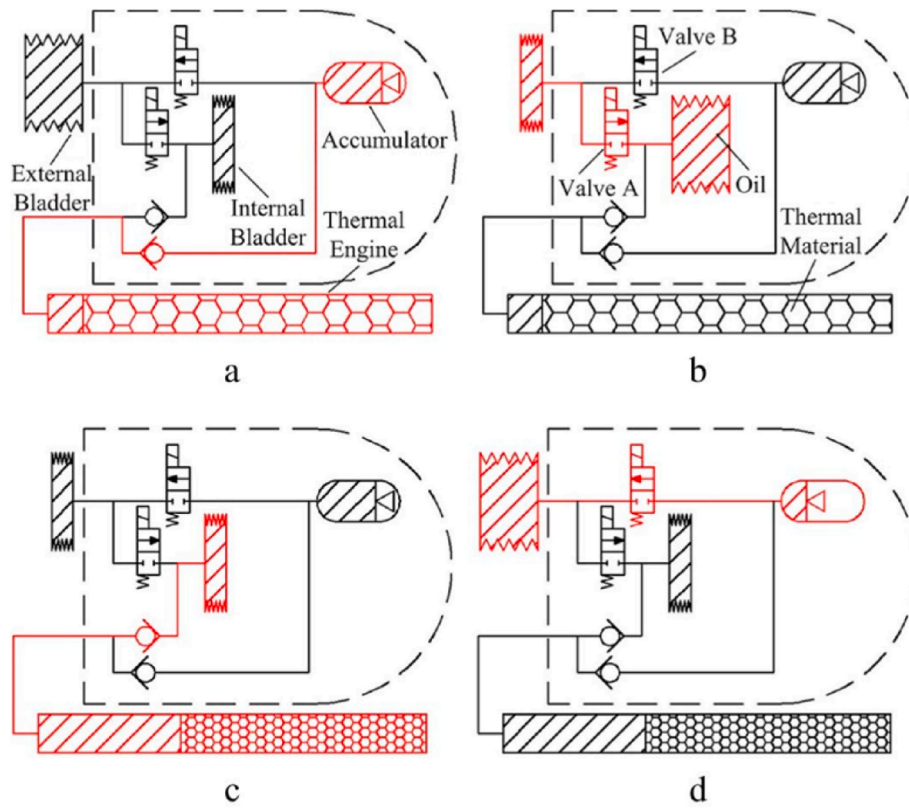


Fig. 4. The mechanism of a buoyancy regulation system [18].

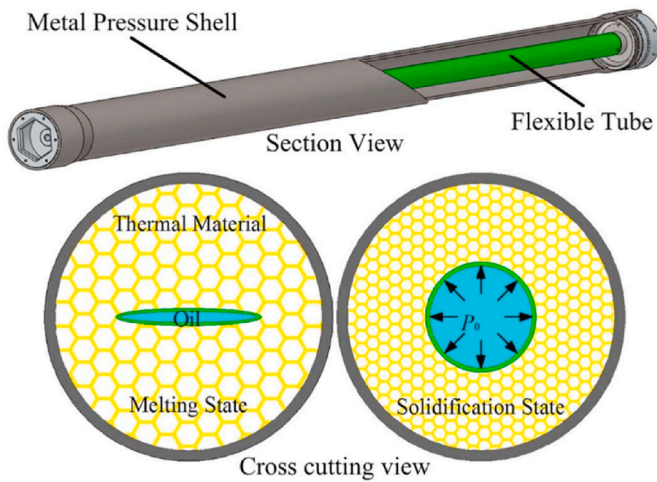


Fig. 5. A thermal engine with a double-layer structure in a buoyancy regulation type UUV; upper) section view; lower) cross-cutting view [18].

volumetric change for the thermal engine reached 89.2% of the theoretical value in the field test, and the thermal engine provided 124 W of hydraulic output power to control buoyancy. The hydraulic output power is defined as power released by the accumulator, which can last 4 min in each energy cycle profile [24].

The performance of a UUV with PCM-based buoyancy regulation can be evaluated in terms of mission capabilities such as diving depth and mission range. In the literature [18–21], the diving depth and mission range of buoyancy regulation type UUVs in field tests were reported to be 150–1400 m and 677–3000 km, respectively (Table 4). Material availability and durability for PCM engines are critically important for PCM-based buoyancy regulating UUVs. Kuznik et al. and Shamberger

and Bruno listed 32 PCM elements for fabricating the PCM materials [25, 26], and Pilon et al. listed 500 commercially available PCMs [27]. Harikrishnan et al. reported an estimated average service life for PCM composites of approximately 13–14 years, considering 5000 thermal cyclic operational conditions for buildings application (Table 4) [28]. However, the lifetime of PCMs in UUV applications has not yet been adequately researched. Without factoring in the cost of a PCM-based buoyancy regulation engine, the anticipated cost of a profiling float UUV is over \$20K and the cost of a glider-type UUV is over \$50K [2,29]. Five PCMs were tested and compared for oceangoing UUVs in laboratory environments, and dodecane ( $C_{12}H_{26}$ ) was shown to have the highest thermal-to-hydraulic conversion efficiency of 4.36% [30]. Based on the material price of dodecane (\$152/kg), the raw material cost for a PCM that would be used in a buoyancy regulation engine (3.6 kg) for a glider is approximately \$547, which is insignificant compared to the overall cost of a PCM engine or UUV (Table 4) [18,31].

### 3.1.2. Electrical energy storage

Buoyancy regulation can provide mechanical power for vertical propulsion of the UUVs, but electrical power is still required to power the sensors in UUVs. The number and variety of sensors in UUVs have increased to meet the need for improved ocean observations, thereby increasing the UUV electrical power requirement. Since the 2000s, researchers have studied electrical energy storage for UUVs based on PCMs which utilize ocean thermal-electricity conversion technologies [9]. Fig. 6 shows the mechanism of the electrical energy storage system in a UUV; it is similar to the buoyancy regulation type, but the hydraulic motor, electric charging system, and battery are additionally used in mechanical-to-electrical conversion to power the buoyancy regulation system, sensors, and wireless communication systems [24].

At the surface, PCM in the thermal engine maintains a liquid state where surface temperature is higher than melting point of PCM, and a bladder is filled with hydraulic oil (Fig. 6a). As the PCM-based UUV descends, the water temperature decreases gradually. As the PCM's

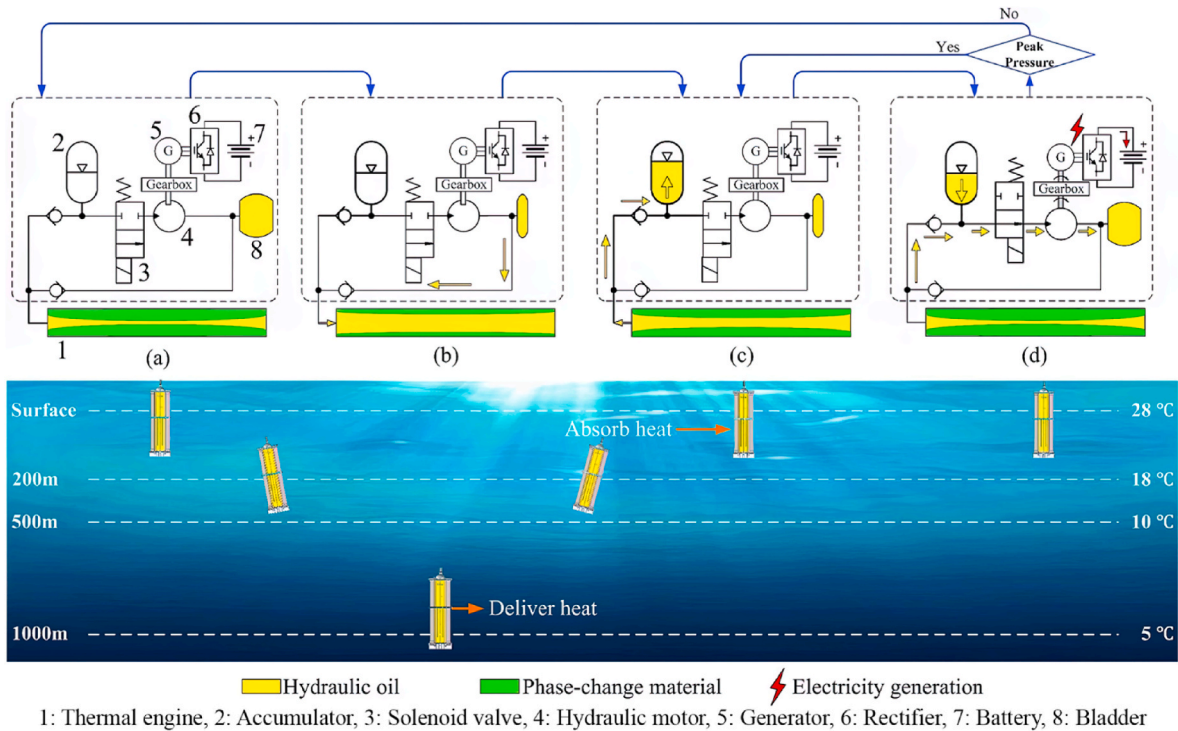


Fig. 6. Schematic of PCM-based electrical energy storage [24].

freezing point is passed, the oil in the bladder passes into the thermal engine (Fig. 6b). When the PCM-based UUV ascends, the water temperature gradually increases. When the PCM's melting point is passed, the PCM exerts pressure on the oil causing it to flow into the accumulator that is storing the hydraulic energy (Fig. 6c). When the predefined maximum pressure in the accumulator is reached, the solenoid valve is opened and the oil flows from the accumulator into the hydraulic motor. The hydraulic motor in turn converts the hydraulic energy into rotational mechanical energy to rotate the generator. The generator produces electrical energy to charge the battery (Fig. 6d). When the predefined minimum pressure in the accumulator is reached, the solenoid valve is closed, completing one energy-generation cycle.

For PCM-based electrical energy storage type UUVs, the energy conversion process consists of three steps: thermal-to-hydraulic energy conversion, hydraulic-to-kinetic energy conversion, and kinetic-to-battery energy conversion [24]. The total energy conversion efficiency

(thermal-to-battery energy) of electrical energy storage type PCM-based UUVs is 0.14–0.59% [9,24,32,33]. Reported energy outputs (Table 4) are 1.7–2.2 Wh in each energy cycle profile and, considering the mass of PCM, energy storage densities (defined as the ratio of generated electrical energy to weight of PCM) are 0.17–0.31 Wh/kg (Table 4) [9,24,32,34,35]. Field tests of PCM-based electrical energy storage type UUVs have been conducted since 2009. The NASA Jet Propulsion Laboratory (JPL) attempted to develop a SOLO-TREC profiling float that would generate electricity from ocean thermal energy [36]. The device was deployed near Hawaii and operated without failure from November 2009 to June 2011. The second-generation of the JPL glider (Slocum-TREC glider) that was developed with Teledyne Webb Research was deployed on June 9, 2015 off the coast of the U.S. Virgin Islands [32]. Field test results from the Slocum-TREC glider show that it dove to 1200 m and generated 1.8 Wh per dive. Tianjin University developed an electrical-storage type glider (OTEC-PCM) and conducted a field test in

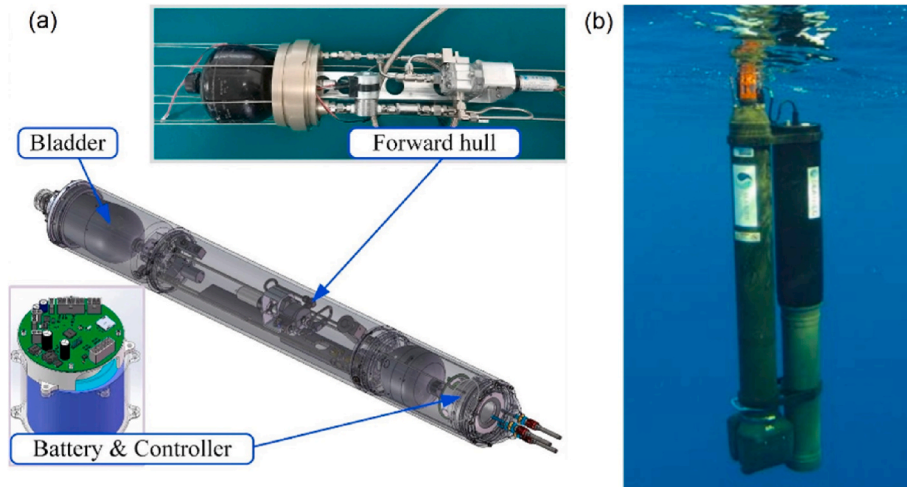


Fig. 7. (a) Section view of OTEC-PCM [24] and (b) deployment of Navis-SL1 [37].

the South China Sea [24]. Using a low PCM mass of (6 kg), during each energy cycle profile their prototype generated 1.86 Wh demonstrating excellent performance (Fig. 7a) [24]. The Navis-SL1 profiling float-type UUV developed by SEATREC Inc, is commercially available (Fig. 7b), and generated 2.2 Wh per dive at a maximum operating depth of 1000 m in a field test [37]. In the literature [24,32,34,38], the diving depth and mission range of electrical energy storage type PCM-based UUVs in field tests were reported to be 150–1200 m and 3280 km, respectively (Table 4).

### 3.1.3. Thermal conductivity of PCMs

A PCM-based UUV has been demonstrated to travel 3000 km per deployment in a field test [18]. However, the generated energy per profile is only half of the energy consumption of a UUV (2.8–4.4 Wh per profile). This challenge may be addressed by accelerating the phase transition process so that a shorter time is needed to transfer the same amount of stored energy and a higher volume expansion rate can be achieved.

One of the challenges for the PCM used in UUV for ocean exploration is that the thermal conductivities of PCM with appropriate melting temperatures are low. For example, hexadecane ( $C_{16}H_{34}$ ) has been identified as a good PCM candidate for UUV application (melting temperature 18 °C) and its thermal conductivity is 0.33 W/(m·K) at 5 °C and 0.14 W/(m·K) at 28 °C [39]. The two temperatures, 5 °C and 28 °C, are for the seawater at 1000 m depth and at the surface [40]. Meanwhile, a 3.25% thermal-to-hydraulic conversion efficiency was achieved using another *n*-alkane tetradecane ( $C_{14}H_{30}$ ) as the PCM for ocean thermal energy conversion (OTEC) applications. However, tetradecane has a thermal conductivity of 0.13 W/(m·K) at room temperature, which will lead to a slower charging/discharging rate and a low generated energy per cycle [24]. The thermal properties of some common *n*-alkane PCM are summarized in Table 2.

The heat transfer rate can be improved by increasing the PCM's thermal conductivity. There are some extensive reviews for enhancing the thermal conductivity for PCMs [45,46]. The tube-fin arrangement has been used to improve the PCM's effective thermal conductivity in UUVs. An aluminum metal fin positioned radially in a container filled with polyethylene glycol (PEG)-1000 was found to increase the effective thermal conductivity of pure PEG-1000 by 42 times. A similar carbon fin structure was found to increase the thermal conductivity by 33 times [47]. However, a significant amount of mass (34–42 wt%) and volume (23–25 vol%) will be occupied by the fin structure, which is an issue for UUVs in which space and payload are limited.

Another method for increasing the thermal conductivity is to fabricate a PCM composite where the PCM flows into the pores of the high thermal conductivity supporting materials. PCM composites are usually

**Table 2**  
Common *n*-alkane PCM candidate for UUV used in ocean exploration.

<i>n</i> -alkane PCM	Approximate Melting Temperature (°C)	Thermal Conductivity at Melting Temperature (W/(m·K))	Enthalpy of Phase Change (solid to liquid) (kJ/kg)	Reference
Tetradecane ( $C_{14}H_{30}$ )	6	0.13	215.7	[41]
Pentadecane ( $C_{15}H_{32}$ )	10	0.147	161.3	[42]
Hexadecane ( $C_{16}H_{34}$ )	18	0.146	234.5	[41,43]
Heptadecane ( $C_{17}H_{36}$ )	22	0.146	164.2	[41,42]
Octadecane ( $C_{18}H_{38}$ )	28	0.15	236.6	[41,43]
Nonadecane ( $C_{19}H_{40}$ )	32	0.152	168.1	[43,44]

fabricated by embedding a PCM in a porous supporting matrix or polymer to increase the thermal conductivity and overcome the leakage issues during repeated melting and solidification processes [48]. Wang's group developed a series of PCM composites using oriented graphite sheets, reticulated graphite nanoplatelets and copper foam to reduce the junction thermal resistance between separated nanoparticles in the case of simple mixing of PCM and additives with high thermal conductivity [49–53].

Atinafu et al. encapsulated a myristic acid (MA)/stearic acid (SA) mixture into an N-doped porous carbon matrix [54]. The formed composite had a resulting thermal conductivity that doubles that of the pristine PCM, as shown in Fig. 8. The introduction of the N heteroatom changed the textural properties of carbon and is thought to be a key component in the formation of a heat transfer network [54]. In many other studies published on this topic, graphene, carbon nanotubes were used as the encapsulation shells to enhance the thermal conductivity [55–58]. This encapsulation strategy is suitable for energy storage applications of PCMs, where the thermal conductivity can be effectively increased by the porous support and the leaking of PCMs can be minimized by restricting the PCM inside the pores of the support. However, encapsulating PCMs into porous support is not suitable for the application of powering UUVs where the volume change of PCMs during melting is needed for power generation.

The other method for increasing the PCM's thermal conductivity is to use additives (0D nanoparticles such as  $TiO_2$  and 1D materials such as graphite fiber and carbon nanotubes) that have high thermal conductivity to the PCMs. This addition helps to form a heat conduction network, which can improve the thermal conductivity, while minimizing the additional mass, by increasing the phonon mean free path.  $TiO_2$  was added to paraffin in a study and resulted in a thermal conductivity increase of 47.85% for the paraffin containing 3 wt percent (wt %) of the  $TiO_2$ . Sodium stearoyl lactylate was found to improve the thermal stability of the  $TiO_2$ /paraffin composite and to improve the dispersion of the nanoparticles [59].

Multiwall carbon nanotubes (MWCNTs) are another effective additive for increasing the PCM's thermal conductivity. Warzoha and Fleischer added MWCNTs of different diameters to IGI 1230A paraffin, and the measured thermal conductivity enhancement results are summarized in Fig. 9. The MWCNT/paraffin nanocomposites' bulk thermal conductivity increased from about 20% to 170% with loadings of MWCNTs from 0.5 vol percent (vol%) to 5 vol%. Moreover, the MWCNT/paraffin composites' thermal conductivity enhancement was demonstrated to increase as the diameter of MWCNTs increased, because of the much higher contact areas between MWCNTs of larger diameter. It is critical to have enough contact areas between the nano-sized additives so that the interfacial resistances will not limit thermal transport at nanoparticle junctions [60].

Many other studies report the enhancement of the thermal conductivities of PCMs using various additives [61–63]. PCMs with enhanced thermal conductivity will have more efficient heat transfer during the phase change, which can help increase the power output for a PCM-based UUV. According to a parametric study, the time needed for phase change can be reduced by 35% when the PCM's thermal conductivity doubles [64]. In another study, the liquid fraction of the organic PCM was shown to have doubled at the same time with only 1–5 wt% additive of material that has high thermal conductivity [65]. It was reported that the freezing rate of the stearic acid increased over 90% when 5 vol% MWCNT was added with some dispersion agent such as poly vinyl pyrrolidone (PVP) [66]. The power generation per profile of a UUV using PCM technology may double if the PCM's thermal conductivity can be increased 2–4 times using less than 5 vol% additives that have high thermal conductivity.

### 3.2. Shape memory alloys-based UUVs

Shape memory alloys (SMAs) can be deformed at low temperatures

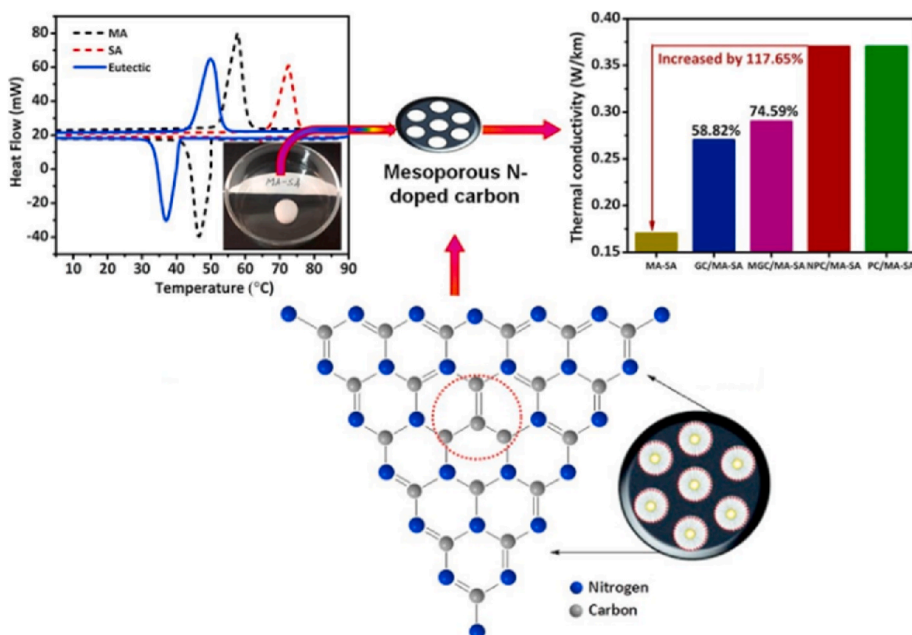


Fig. 8. Heat flow (upper-left) and thermal conductivity (upper-right) of porous carbon matrix/MA-SA composite PCMs [54].

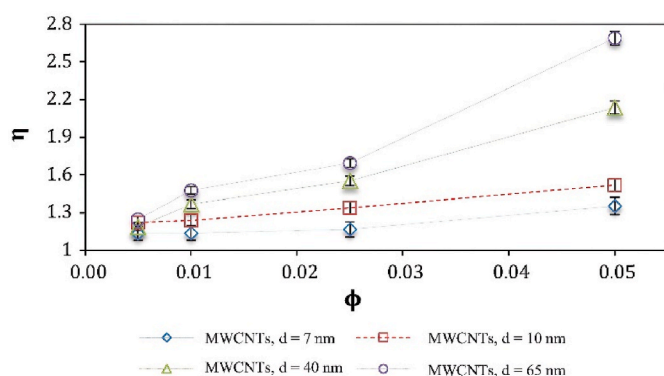


Fig. 9. Thermal conductivity enhancement of paraffin using MWCNTs that have different diameters and concentrations.  $\eta$  is the ratio of the thermal conductivity between the MWCNT/paraffin composition and the intrinsic paraffin [60].

but when heated to a critical temperature return to their original shape. The buoyancy of a UUV can be directly controlled by the deformation of an SMA (Fig. 10). In warmer surface water, the SMA contracts, making the UUV negatively buoyant and causing it to dive. As the threshold temperature where the SMA starts to elongate is passed, the UUV becomes positively buoyant causing it to ascend.

The laboratory tests of an SMA-based UUV have demonstrated that by varying in the length of nitinol (NiTi) wire SMA, induced by temperature differences, altered the devices buoyancy successfully [67]. Angilella et al. built a buoyancy engine prototype based on SMA (Fig. 11) for a conceptual UUV, evaluated its performance in a laboratory water bath, and calibrated it relative to simulated temperature-displacement behavior [68,69].

The estimated energy storage density of SMA-based UUVs is 0.33 Wh/kg (Table 4) [9]. However, there are no reported field tests of an SMA-based UUV. The material selection availability and durability of SMAs are key considerations for an SMA-based UUV. Barbarino et al. described 16 elements for fabricating the SMA materials using various compositions [70]. In the commercial market, over 20 commercial SMA materials are available (Table 4) [71–77], with the most widely used

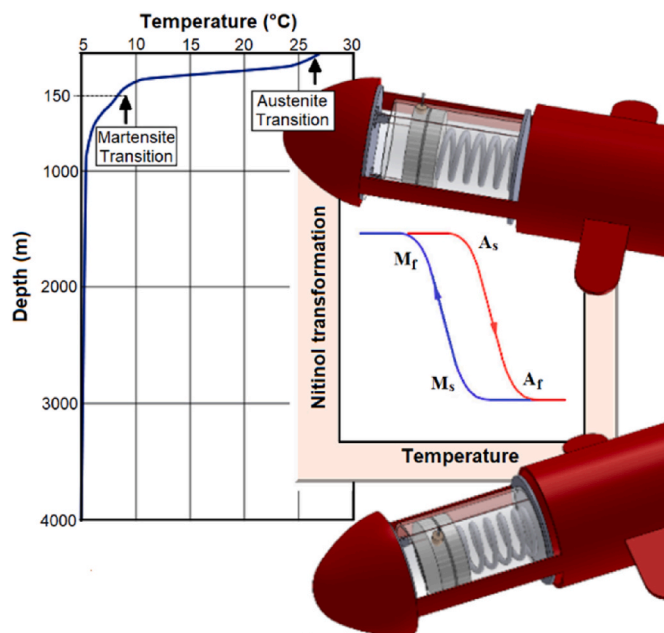


Fig. 10. Schematic of an SMA system for UUVs [67].

SMA material being NiTi [78]. Yang et al. reviewed NiTi, an alloy that features high corrosion resistance, and reported that NiTi showed the highest maximum recoverable strain (8%) among the most popular SMAs (NiTi, Cu–Al–Ni, and Cu–Zn–Al) [79]. Johnson Matthey Inc. reported the thermal cycles of NiTi with different transformation strains, which can be over 100,000 cycles as 4% of transformation strain is applied (Table 4) [80]. However, the lifetime of SMAs in UUV applications has not yet been adequately researched. Angilella et al. reported that 2 kg of NiTi SMA wire is required to dive up to a 1 km depth subsea based on a preliminary laboratory test [68]. The SMA raw material cost for the NiTi that would be used in a buoyancy regulation engine for a UUV is approximately \$1800 (Table 4), based on the material price of NiTi SMA material (\$900/kg, Nexmetal Corporation) [81].

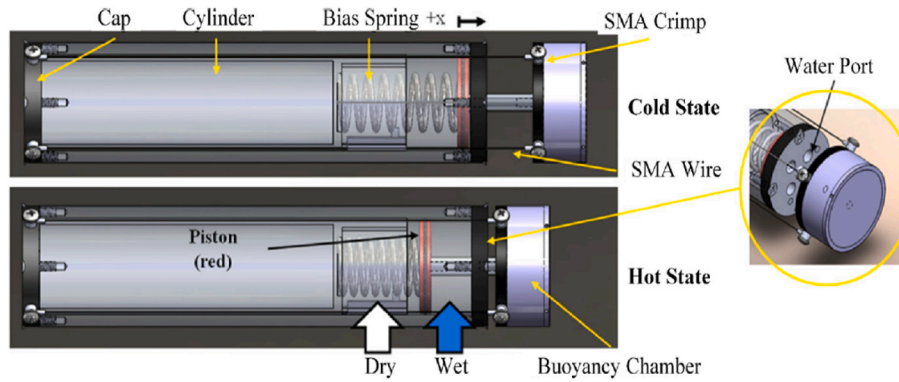


Fig. 11. Schematic of an SMA system for UUVs [69].

### 3.3. Thermoelectric generator-based UUVs

Thermoelectric generators (TEGs) directly convert thermal energy to electrical energy using the Seebeck effect of thermoelectric materials. A TEG-based UUV uses thermal storage such as PCM, which is in indirect contact with the surrounding fluid, to generate a temperature difference for power generation in the ocean (Fig. 12). At the surface of the ocean (Fig. 12a), the upper side of a TEG has a higher temperature than the bottom side that is in contact with the thermal storage. When the UUV dives and reaches depth (Fig. 12b), the upper side of the TEG has a lower temperature than the bottom side due to the thermal storage. The thermal gradient between the stored, insulated material and the exterior temperature at depth generates power for a UUV using the TEG.

The advantages of TEGs are reliability smooth operation, and simplicity, but TEGs are only at the conceptual research phase for UUV applications [82,83]. To study the feasibility of oceanic applications, Carneiro and Almeida developed a conceptual design of a TEG-based UUV using theoretical calculations and subsea thermal profiles (Fig. 13), and discussed the estimation of the efficiency, energy storage density, and required TEG and PCM size [84].

Carneiro and Almeida [84] reported the TEG-based UUV's total energy conversion efficiency in the simulation was 0.1% based on the energy conversion efficiency definition of TEG systems, which Dewan et al. [85] defined as the ratio of electrical power to the heat flux through the thermoelectric module. Carneiro and Almeida also estimated the energy storage density of a TEG-based UUV to be 0.058 Wh/kg (Table 4), which is the lowest energy density among the five thermal gradient generators [84]. The material selection availability and durability of TEGs are important considerations. Selvan et al. listed the 73 available thermoelements for manufacturing the TEGs [86]. Wang et al. reported that the total thermal cycle of a TEG to be 42,000 before failure

(Table 4) [87]. The lifespan of a thermoelectric module is 200,000 to 300,000 h, and a module can last for more than 100,000 h of continuous operation (Table 4) [88–90]. However, the lifetime of TEGs in UUV applications has not yet been adequately researched. Simulation results of TEG-based UUVs over the temperature variations to depth of 1200 m (from 26 °C to 4.2 °C), demonstrate that a mass of 28.9 kg of PCM storage and a contact area of 0.05 m<sup>2</sup> for the TEG allow for the extraction of the energy required per each 1200 m dive (6 kJ) [84]. Thus, 55 TEGs (TEG1-1263-4.3, TECTEG, Canada) and 28.9 kg of PCM are required to power a UUV, which would cost \$1200 and \$4,390, respectively, for the raw components (Table 4) [91].

### 3.4. Thermodynamic cycle-based UUVs

#### 3.4.1. Miniaturization of thermodynamic cycles used for OTEC

The thermodynamic cycle system for OTEC is somewhat mature for large-scale ocean thermal energy harvesting equipment. The miniaturization of OTEC has been studied by several researchers [92,93], but for UUV applications, thermodynamic cycle-based UUVs have not advanced beyond the conceptual research phase. Howard designed a thermodynamic cycle-based UUV using the Rankine cycle (Fig. 14) [94]. In their design, warm surface seawater and cold deep seawater are used as heat exchangers, and the thermal energy is stored using a thermal mass to generate the temperature difference for power generation. The Brayton cycle has many similarities to the Rankine cycle, with the exception of no phase change in the cycle's working gas. A Brayton cycle-based UUV was conceptually designed and operates utilizing the temperature difference between the surface air and deep water [93].

The definition of the thermodynamic cycle system's energy conversion efficiency is the ratio between the input heat capacity and the net power from the turbine. The thermodynamic cycle system for a large-

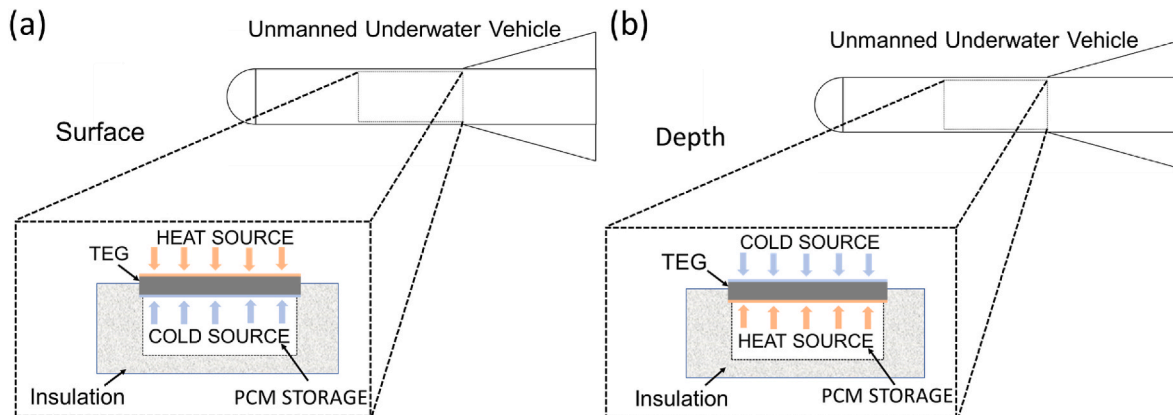


Fig. 12. Conceptual design of a TEG system for UUVs.

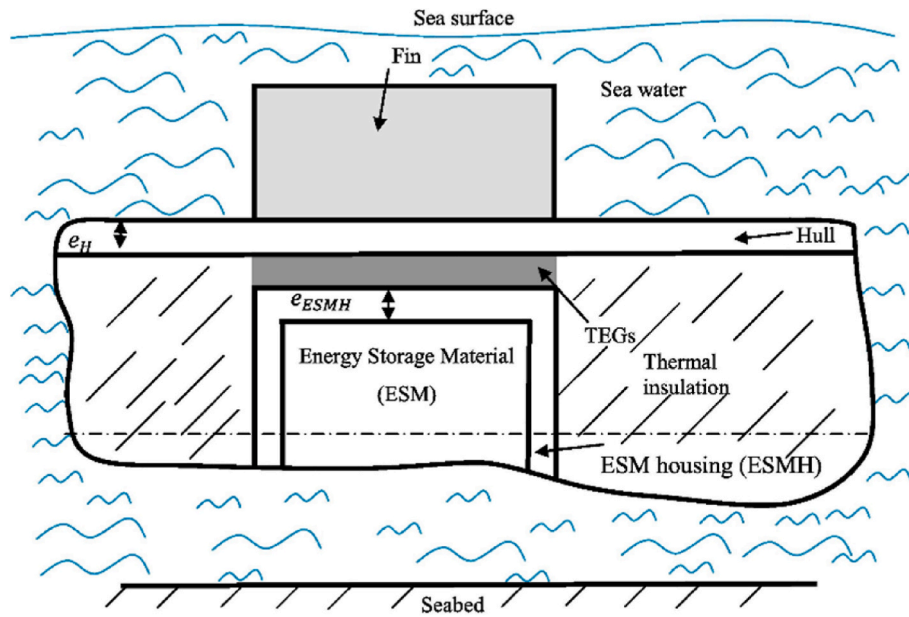


Fig. 13. Conceptual design of a TEG system for UUVs [84].

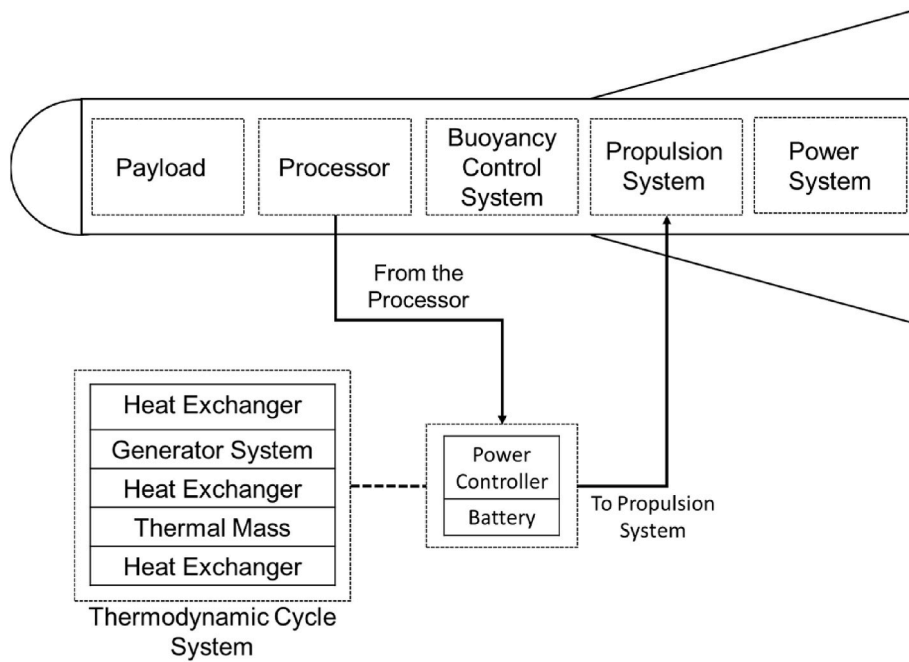


Fig. 14. Conceptual design of a thermodynamic cycle system, using the Rankine cycle for UUVs [94].

scale power plant has a reported theoretical efficiency that is up to 4% [95], but the efficiency in UUV applications has not yet been reported in the literature. The estimated energy storage density of thermodynamic cycle-based UUVs is 0.085 Wh/kg (Table 4) [9]. The lifetime of a thermodynamic cycle system is more than 20 years for a large-scale power plant, but the lifetime of a thermodynamic cycle system in UUV applications has not yet been adequately researched [96]. The cost of a 50 MW thermodynamic cycle system for OTEC was reported (\$75 M), but there is no reported information regarding the cost of small-scale thermodynamic cycle systems suitable for UUVs [97].

### 3.4.2. Stirling engines for UUVs

A Stirling Engine converts thermal energy into mechanical work to form a heat engine. Although Stirling Engines have not been developed

for UUV applications, they could potentially generate energy from the thermal gradients in the ocean to power UUVs. There are many varieties of Stirling Engine that use different geometric configurations, such as alpha, beta, and gamma types. A gamma-type Stirling Engine is illustrated below (Fig. 15) and comprises the following components: a power piston that is forced to move by the compression and expansion of the gas and thereby generates power; a displacer piston that moves gas between the hot side (in this case on the bottom of the engine) and the cold side; a regenerator that recycles heat in the engine; an external heat source; and an external heat sink. The two pistons are connected to crankshafts that link to a flywheel; the flywheel's momentum keeps the engine running. The crankshafts are connected to different points on the flywheel so that the displacer piston and power piston operate out of phase with one other.

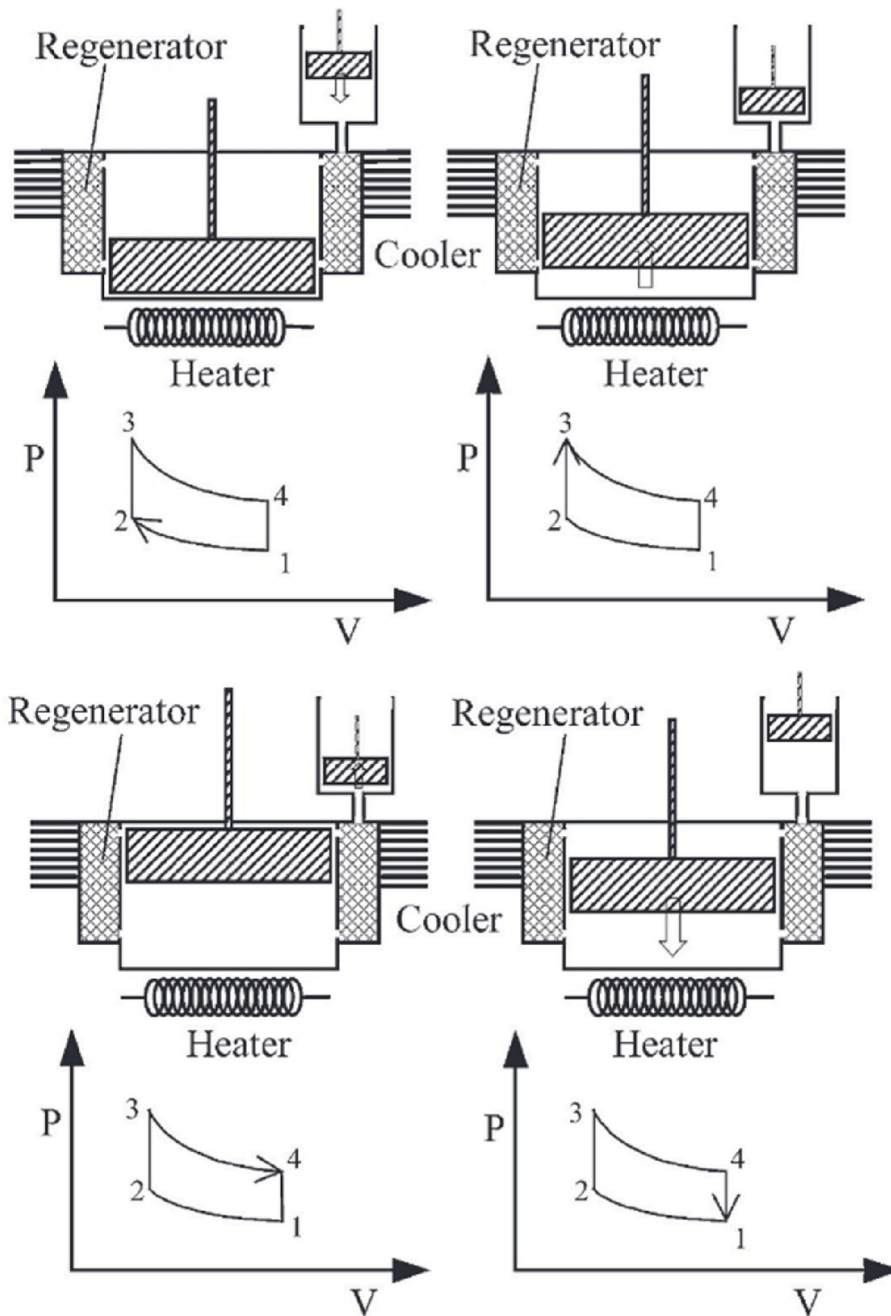


Fig. 15. Illustration showing the geometry and operation principle of a gamma-type Stirling Engine [98].

To generate power from temperature differences that occur over a large distance in the ocean, the Stirling Engine must include thermal storage. The thermal storage can be used to act as either a heat source or sink depending on the location of the UUV. PCMs are suitable for the storage media since heat addition and removal from the Stirling Engine is isothermal, as is the phase change of the PCM.

An example schematic of a Stirling Engine integrated with PCM thermal storage is shown in Fig. 16. When the float is at the surface, the warm water near the surface is used as the engine's heat source and also used to charge (melt) the hot PCM. The cold PCM is solid, having been frozen earlier by cold seawater at depth, and is used as the heat sink. When the float descends, the melted hot PCM is used as the heat source, while heat is exchanged with cold seawater, which also cools/freezes the cold PCM.

Stirling Engines have not been developed for ocean applications, and

systems referred to as "low-temperature difference" Stirling Engines typically have heat source temperatures of around 100 °C and are intended for applications such as waste heat recovery. These systems typically have efficiencies in the range of 1–2% (Table 3). Martaj et al. developed a Stirling Engine that operated with a temperature difference of ~11 °C (which is similar to ocean thermal gradients) and obtained an efficiency of 0.28% [99].

The performance of low-temperature difference Stirling Engines can be estimated using simple thermodynamic models. The simplest model assumes that compression and expansion occur isothermally and that the main loss occurs in the regenerator, which is characterized by an effectiveness  $\epsilon$ . The efficiency  $\eta_{\text{isothermal}}$  is given by

$$\eta_{\text{isothermal}} = \frac{(\gamma - 1)(\tau - 1) \ln r}{(\gamma - 1)\tau \ln r + (1 - \epsilon)(\tau - 1)} \quad (1)$$

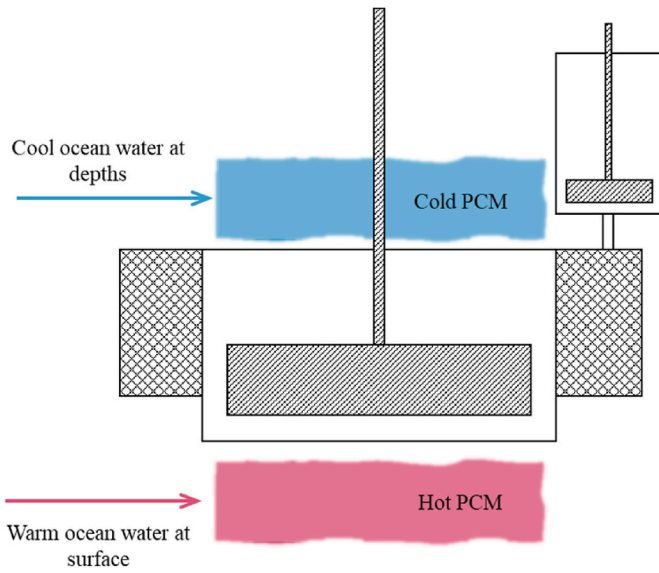


**Fig. 16.** Example schematic of a Stirling Engine integrated with PCM thermal storage that is charged by hot or cold seawater.

**Table 3**  
Performance of low temperature difference Stirling Engines.

$T_h, ^\circ\text{C}$	$T_c, ^\circ\text{C}$	HX Effectiveness	Volume Ratio	Efficiency, %	Reference
120	20	0.5	1.04	2.27	[100]
70	20	–	1.06	1.3	[101]
130	–	–	–	3.5	[102]
23.3	12.6	0.5	1.01	0.28	[99]

where  $\gamma = c_p/c_v$  is the ratio of specific heats,  $\tau = T_h/T_c$  is the ratio of the heat source and sink temperatures, and  $r = V_{max}/V_{min}$  is the compression ratio.

This expression can be improved by noting that the compressions and expansions that occur are unlikely to be isothermal and instead may be adiabatic; i.e., the temperature will vary polytropically due to compression and expansion. This assumption produces the expression:

$$\eta_{adiabatic} = \frac{\tau(1 - 1/r^{\gamma-1}) - r^{\gamma-1} + 1}{\tau(1 - 1/r^{\gamma-1}) + (\tau - 1)(\epsilon - 1)} \quad (2)$$

An alternative model considered “endo-reversible” thermodynamics, or finite-time thermodynamics [103]. Unlike Carnot analysis, which

assumes that heat engines operate between the source temperature  $T_h$  and sink temperature  $T_c$ , endo-reversible analysis acknowledges that there must be a difference in temperature between the source temperature and the actual temperature within the hot space of the Stirling Engine in order for heat to be transferred to the engine. The same will occur in the cold space. Therefore, the Stirling Engine actually operates over a temperature range smaller than  $\tau = T_h/T_c$ . The analysis presented by Kaushik et al. calculates the efficiency  $\eta_{endo}$  under the assumption that the power output is maximized, which leads to the following expression [103]:

$$\eta_{endo} = \frac{1 - \sqrt{T_c/T_h}}{1 + \frac{(1 - \epsilon)}{(\gamma - 1)\ln r} [1 - \sqrt{T_c/T_h}]} \quad (3)$$

Note, that in the case  $\epsilon = 1$ , Eq. (3) reduces to the Chambadal-Novikov efficiency (sometimes called Chambadal-Novikov-Curzon-Ahlborn efficiency), which is the conventional result of applying endo-reversible thermodynamics to a heat engine and is considered to be a more accurate estimate of heat engine performance than the Carnot efficiency.

These three models are compared in Fig. 17 for Stirling Engines using air as the working fluid for a range of compression ratios and regenerator effectiveness. The temperature difference is 20 °C which is a value that is possible in the ocean. The figure indicates that the performance is sensitive to the value of regenerator effectiveness, which indicates the design of this component is a key consideration. The isothermal and endo-reversible models indicate that the maximum efficiency occurs at infinite compression ratios, whereas the adiabatic model predicts an optimal volume ratio. All three models show reasonably good agreement at small compression ratios, but they differ significantly in their estimates of the optimal efficiency which suggests further modelling efforts are required. It should be noted that additional inefficiencies will occur in real systems, so the results in Fig. 17 should be considered to be optimistic. For the system illustrated in Fig. 16, it will be important to understand any losses that arise from using PCM thermal storage as the heat source and sink.

### 3.5. Current technology limitations

Currently, the technology to harvest the available temperature gradient energy is inadequate for long-term powering of UUVs. The maximum temperature difference in the Indian Ocean is 20 °C [9] Field testing of a PCM-based thermal gradient system demonstrated the feasibility of long-lasting mission of UUVs [11], but the output power is not enough to power a UUV with an autonomous sensing system (1.1–14.7 Wh per profile) [2–4,8,10–15]. The main drawback of a

**Table 4**  
Summary of technologies that use thermal gradient energy to power UUVs.

Type	Phase Change Material (PCM)-based UUVs		Shape Memory Alloys (SMA)-based UUVs	Thermoelectric Generator (TEG)-based UUVs	Thermodynamic Cycle-based UUVs
	Buoyancy Regulation	Electrical Energy Storage			
Energy Generation (Wh)	N/A	1.7–2.2	N/A	N/A	N/A
Energy Storage Density (Wh/kg)	N/A	0.17–0.31	0.33	0.058	0.085
Efficiency (%)	0.29–0.33	0.14–0.59	N/A	0.1	N/A
Field Test	Y	Y	N (Lab test)	N (Concept)	N (Concept)
Depth (m)/Range (km)	150–1400/ 677–3000	300–1200/3280	N/A	N/A	N/A
Materials Selection Availability	>32 PCM elements		>16 SMA elements	>73 Thermoelements	N/A
Durability (Lifetime)	PCM: 13–14 years, >5000 cycles		>100,000 Thermal cycles	TEG: 200,000–300,000 h, >42,000 thermal cycles,	Thermodynamic cycle system: >20 years
Anticipated Raw Material Costs	PCM engine materials (\$547)	PCM engine materials (\$912)	SMA engine materials (\$1800)	TEG materials (\$1200) + PCM thermal storage (\$4300)	Thermodynamic cycle engine materials (?)
Key Reference	[18]	[24]	[68]	[84]	[94]

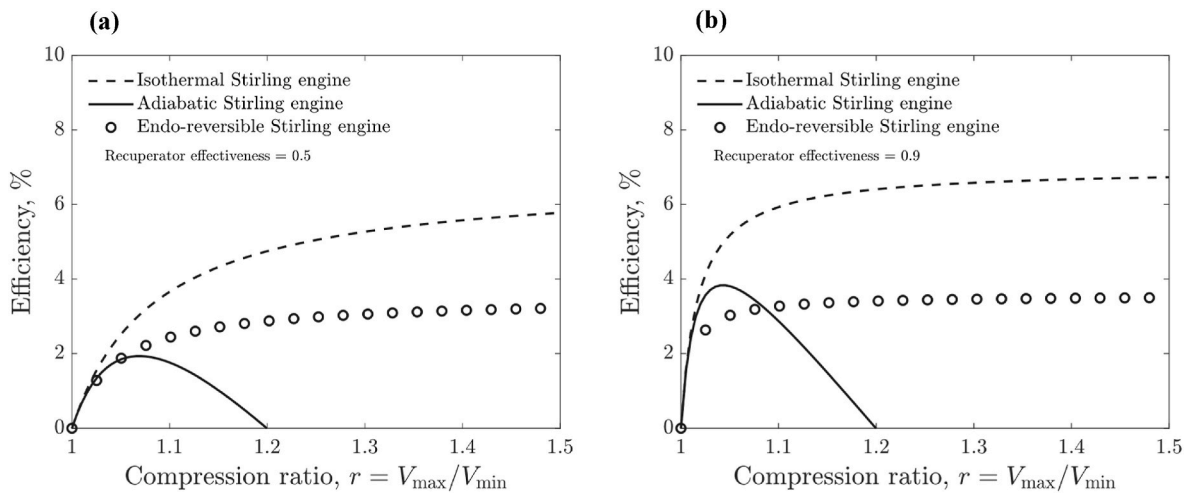


Fig. 17. Efficiency of Stirling Engines using several thermodynamic models. Air is the working fluid, and  $T_h - T_c$  is 20 °C, recuperator effectiveness is (a) 0.5, (b) 0.9.

PCM-based system is its low efficiency. The thermal-electrical efficiency is less than 0.6%, and the thermal-mechanical efficiency is less than 0.4% [20,24]. The challenges associated with PCM-based thermal energy harvesting technology are slow heat transfer rates and low energy storage density (0.31 Wh/kg) compared to the energy storage density of a battery cell (30–260 Wh/kg) [104]. Taking into account the need for maintenance, PCM-based UUVs are complex systems that consist of a hydraulic system, a mechanical and electrical system, and a storage device, which raise the likelihood of failure [9]. In the case of a TEG-based UUV, the theoretical maximum efficiency using one of the most efficient TEG material ( $\text{Bi}_2\text{Te}_3$ ) is only 1.67%, for a deep sea temperature of 4 °C and an ocean surface temperature of 27 °C [85]. In the case of OTEC systems, a pump is required to move the deep seawater to the ocean surface. As a result there is a significant reduction in extractable energy [105]. The implementation of these cycles in UUVs needs further investigation. The ocean thermal gradient energy systems based on SMA are currently only at the lab testing stage. The ocean thermal gradient energy systems based on TEGs and thermodynamic cycle for UUVs are still at the early phase of demonstrating feasibility of components in the laboratory and developing conceptual designs.

Table 5  
Summary of technologies of energy generation from salinity gradients.

	Pressure-Retarded Osmosis (PRO)	Reverse Electrodialysis (RED)	Capacitive Mixing (CapMix)	Microbial Reverse-Electrodialysis Cell (MRC)
Power ( $\text{W}/\text{m}^2$ , membrane area)	0.35–9	0.33–3.8	0.06–0.29 (Electrode area)	1.53–4.3
Salinity gradient (gram/L)	34–35	29–35	29–35	29–35
Flow factor	1.0–32.0 $\text{L}/\text{m}^2\text{h}^1$ (Water flux)	0.56–4.2 $\text{cm}/\text{s}$ (Velocity)	7.5–20.0 $\text{mL}/\text{min}$ (Flow rate)	0.01–0.037 $\text{cm}/\text{s}$ (Velocity)
Efficiency (%) <sup>a</sup>	54–56	18–38	37–54	53–64
Field test	Y (Power Plant)	Y (Power plant)	N (lab test)	N (lab test)
Anticipated cost	\$65–125/MWh	\$90–120 /MWh	N/A	N/A
Viable saline sources	Seawater, concentrated brines	Seawater	N/A	Seawater
Environmental impact	Discharge of chemical effluents, noise	Discharge of chemical effluents	N/A	Discharge of chemical effluents
Key reference	[111]	[114]	[126]	[133]

<sup>a</sup> PRO and RED efficiency [142,143]: Ratio of useful work, W to fraction of Gibbs free energy of mixing ( $\Delta G_{\text{mix}}$ ). CapMix efficiency [126]: Ratio of the output net power production to pumping power and charging power, where the external field was generated and delivered to a cell. MRC efficiency [119,135]: Ratio of the generated output power to maximum theoretical energy output by MRC.

#### 4. Salinity-gradient energy

Salinity gradient energy technologies can be broadly classified into chemical to electrical or chemical to mechanical energy conversion systems, and most approaches rely on extracting energy from salinity gradients across a polymer membrane. A brief description of the various salinity-gradient-based energy-generation technologies is provided in this section and a summary of the state of the art is included in Table 5 (at the end of Section 4.5), following by a feasibility evaluation of powering UUVs using salinity gradients (Section 4.7).

##### 4.1. Pressure-retarded osmosis

Pressure-retarded osmosis (PRO) converts the osmotic pressure difference between two feed solutions into electrical energy using a turbine and generator. PRO consists of a semi-permeable membrane that separates the concentrated and dilute solutions, and the pressure generated by the permeate (water) flow into the concentrated feed chamber results in hydraulic pressure, which is used to mechanically drive a turbine and generate electrical energy (Fig. 18). As a result, the electricity generated

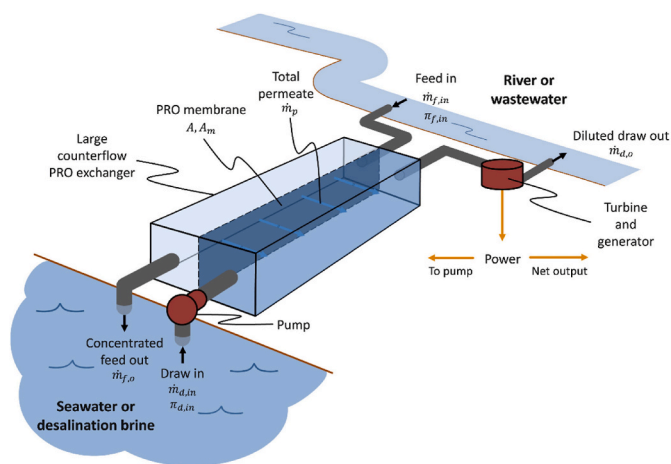


Fig. 18. Schematic of PRO technology [106].

by PRO is directly linked to the difference in concentrations between the feed solutions. Most PRO research has focused on energy generation from seawater and freshwater feeds and has not explored lower salinity-gradient solutions.

PRO performance is generally normalized to the membrane area, and for a seawater-freshwater PRO system, power densities of 0.35–9.0 W/m<sup>2</sup> have been reported (Table 5) [107–109]. Water flux is an important parameter for determining PRO performance because power output is calculated using the differential pressure across the semi-permeable membrane and the water flux through it. Reported water flux in PRO systems ranges from 1.0 to 32.0 L/m<sup>2</sup>h (Table 5) [110,111].

PRO technology is fairly mature in the sense that a 10 kW PRO power plant was successfully field tested in 2009 by Statkraft in Tofte, Norway [112]. However, the system was decommissioned in 2013 because the forecasted power cost of 0.12€/kWh was not competitive in the European power market. One approach to lowering the costs is to use more concentrated brine feeds, such as desalination brine streams, to increase the normalized power output of the semi-permeable membrane. Such integration of PRO with reverse osmosis has been shown to lower the energy consumption from 3.32 to 2.869 kWh/m<sup>3</sup>, and also to reduce the propensity of fouling in PRO membranes [113].

#### 4.2. Reverse electrodialysis

Reverse electrodialysis (RED) is a technology that relies on alternating anion and cation exchange membranes (AEM and CEM) between two electrodes to generate electricity from salinity gradients (Fig. 19).

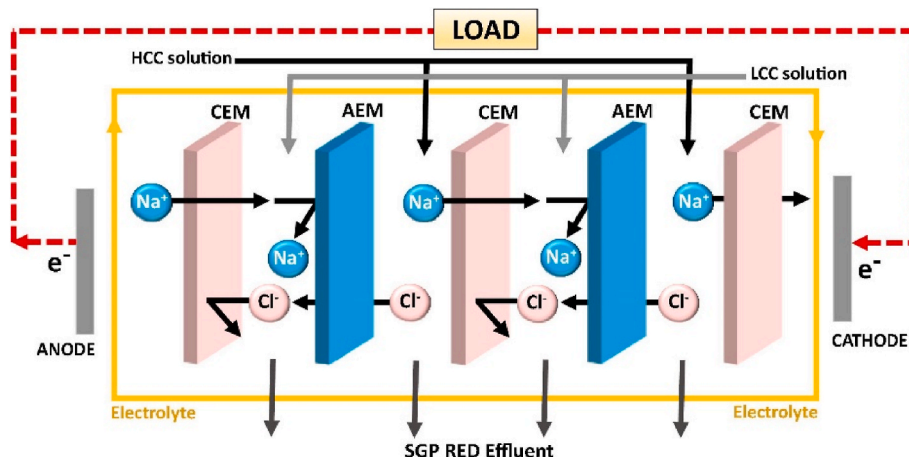


Fig. 19. Schematic of RED technology [114].

The difference in salinity between the two solutions across an ion exchange membrane results in an electric potential gradient that drives anions and cations ions (across the AEM and CEM respectively) from regions of high concentration to those of low concentration. The electrodes then convert the ion flux to electric current by means of either water splitting or a reversible redox reaction [114].

For mixing of freshwater and seawater, RED power densities (normalized to membrane area) of 0.33–3.8 W/m<sup>2</sup> have been reported (Table 5) [115–117]. Hydrodynamics and mass transfer in RED can be affected by the mean fluid flow velocity inside a single channel and reported velocities range from 0.56 to 4.2 cm/s (Table 5) [114,115, 117]. Increasing the feed flow velocity has clear impacts to RED performance, a change in flow velocity from 0.7 to 1.1 cm/s has been shown to result in significant increase in both open-circuit voltage (35%) and power density (47%) [116].

RED is a relatively mature technology; a pilot-scale plant (50 kW) was tested in Afsluitdijk, Netherlands, in 2014 by Fujifilm and the RED stacks [118]. Unlike PRO, where the generated energy scales with the feed salinity, RED is best operated with a seawater-freshwater mix, because RED encounters reduced energy efficiency at higher salinities, such as in brine streams [115]. Although fairly mature, RED practical applications have had limited success due to inefficiencies of the process, caused by electrode overpotentials, ohmic resistances, energy

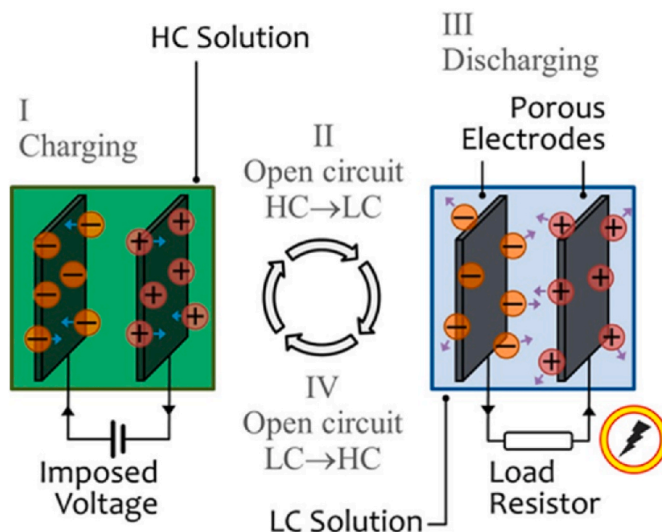


Fig. 20. Schematic of the CapMix technology. Reprinted with permission from Ref. [121]. Copyright 2016 American Chemical Society.

required for pumping, and biofouling [119].

#### 4.3. Capacitive mixing

In capacitive mixing (CapMix), electricity is generated by sequentially exposing high surface area electrodes to high and low salinity solutions, resulting in cycles of electrode charging and discharging (Fig. 20). In a standard operational cycle, (1) flowing an electrical current through the system in a high-salinity solution charges the electrodes; (2) the high-salinity solution is replaced by a lower salinity solution in an open circuit; (3) after closing the circuit an electrical current flows in the direction opposite to the initial step, discharging the electrodes; and (4) the higher salinity solution is returned to the cell for the process to be repeated [120].

Unlike PRO and RED, CapMix is an emerging technology that can be operated without a membrane, making it more attractive for seawater harvesting [122]. However, to increase the potential change when solutions are switched, and to increase the process's overall efficiency, studies have used ion exchange membranes in the system [120]. The reported range of power density for seawater-river water mixing in CapMix is 0.06–0.29 W/m<sup>2</sup> (Table 5) [123–128]. The power density of CapMix increases with flow rate; reported flow rates range from 7.5 to 20.0 mL/min (Table 5) [124,127], with energy efficiencies of 37–54% (Table 5) [126]. However, the energy efficiency significantly decreases at higher salinities because the technology is plagued by undesirable side reactions and electrode degradation. Currently, only laboratory studies of CapMix are reported and, similar to RED, CapMix is best suited for lower salinity sources. Given that CapMix is a cyclic process, the membrane and electrode fouling issues in these systems are believed to be better managed by regularly changing the salinity of the solutions going through the system and by varying the operating conditions to make it difficult for organisms to adapt and grow [129].

#### 4.4. Microbial reverse-electrodialysis cell

Microbial reverse-electrodialysis cell (MRC) technology is a hybrid system derived by combining a RED unit and a microbial fuel cell (MFC) (Fig. 21). An MFC is a bioelectrochemical system that utilizes microbes to generate electrical power from organic matter, from sources like wastewater, while RED generates power from salinity gradients.

The integration of the MFC with RED has advantages in terms of efficiency and power enhancement, as the combination overcomes the limitations of the individual processes [119,131,132]. For example, in an MRC, the RED compensates for the low voltage output of MFC while the voltage generated from microbe-mediated spontaneous reactions in MFC contribute to offsetting energy losses at RED electrodes [133]. Reported power densities obtained by mixing seawater and river water with MRC range from 1.53 to 4.3 W/m<sup>2</sup> [119,131,132,134,135]. Similar to RED, flow rates determine the output power of an MRC system and

have been reported to be 0.01–0.037 cm/s (Table 5) [133]. MRC has only been studied under laboratory conditions to date and no field tests have been reported. However, in the context of energy extracted from salinity-gradients, MRC is expected to be similar to that of RED, but MFC components may need additional operational considerations, given the challenges of managing biofilms in harsh marine environments.

#### 4.5. Hydrogel Expansion

Hydrogel expansion (HEX) is membrane-free salinity gradient energy harvesting method that relies on hydrogels that swell in freshwater and shrink in saltwater, and the expansion/contraction can be used to perform mechanical work (Fig. 22). In general, HEX systems have energy recovery rates lower than PRO and RED [136], and research has been limited to laboratory studies focused on hydrogel development. Various polyelectrolyte hydrogels have been evaluated [136–140], with reported potentials ranging from 0.83 J/g for poly (acrylic acid) to 102 J/g for polysulfobetaine [138,139]. While this variability in energy generation potential is largely due to differences in the hydrogel chemistries,

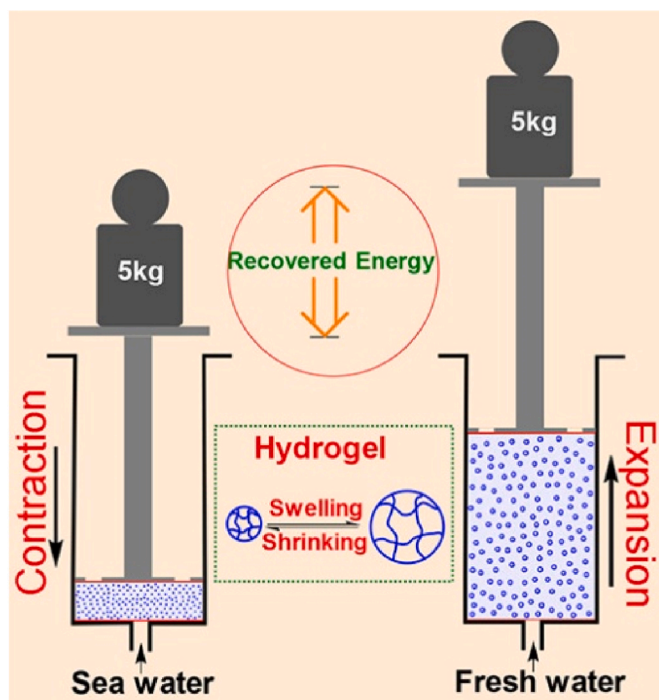


Fig. 22. Schematic of Hydrogel Expansion technology. Reprinted with permission from Ref. [137]. Copyright 2018 American Chemical Society.

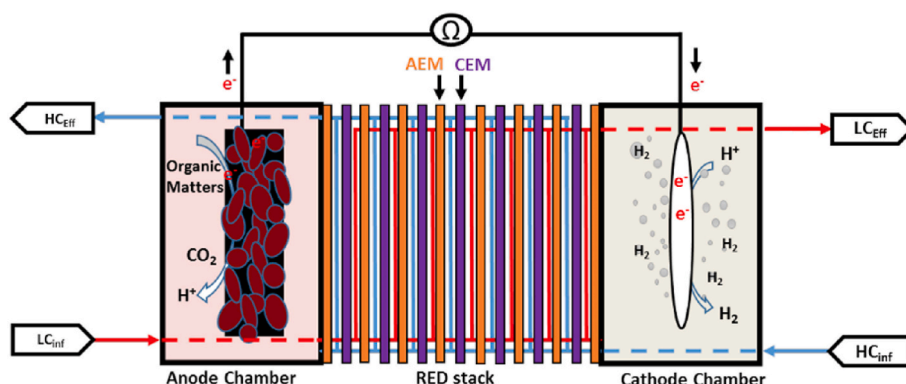


Fig. 21. Schematic of MRC technology [130].

it can also be attributed to the specific system design (e.g., diameter and length of tube holding the gel) used to characterize them. Models suggest hydrogels that deform less can reduce energy loss associated with pumping [141]. However, that would also lead to overall lower energy production from the system—highlighting the need for further development and optimization of HEx method. Given the limited studies on HEx and its being a membrane-less method, clearly distinct from other approaches described here, it is not included in Table 5.

#### 4.6. Current technology limitations

Although demonstrated at powerplant scale, the PRO and RED technologies remain too expensive for wide-spread adoption. The anticipated cost of a PRO plant is USD 65–125/MWh [144], while the RED system is estimated to cost USD 90–120/MWh [144,145]. The high cost is largely due to the cost of the system components required to operate in harsh saline conditions. For example, nearly all salinity-gradient power generation technologies rely on ion exchange membranes, which are vulnerable to scaling and fouling under operating conditions [146]. Existing approaches to minimizing fouling rely on pretreatment of feedwaters and regular chemical treatment of the membranes [147]. Both of these practices add to the capital and operating expenditures of the process, and more importantly, they are not viable strategies for technologies that are used to power UUVs, where system size and weight are critical considerations. While research efforts in the development of antifouling and more robust membranes have been significant, there is not enough information about the fouling of these membranes in ocean settings. Given the environmental and practical considerations surrounding chemical membrane defouling, development of more robust membranes is critical. Similarly, electrode materials that are inexpensive and can operate under marine conditions are required for RED, CapMix, and MRC. Specific to HEx technology, research and optimization of hydrogel polymers is essential. In general, significant research and development of materials, device architectures, operational schemes, and integration of ancillary equipment (pumps, storage tanks, etc.) are necessary before these emerging technologies can be used for extended periods in the ocean to power UUVs, because currently most have only been tested in controlled laboratory environments.

#### 4.7. Salinity-gradient-powered UUVs

The Gibbs free energy of mixing is the theoretical upper bound for the energy available for utilization from mixing two different salinity sources [121]. While Gibbs free energy of mixing does not reflect real losses that would occur in the energy transformations and storage, it is an appropriate parameter to estimate the potential and feasibility of extracting energy from salinity gradients. Unfortunately, all prior reports on Gibbs free energy of mixing look at seawater-river water mixing, which consists of a salinity gradient of up to 35 g/L. Given that for UUVs operating in the middle of the ocean, the available salinity gradients are just 2 g/L over 1 km depth, there is a need to perform feasibility calculations for the low-salinity-gradient case relevant to UUVs. To estimate the energy output from low-salinity gradients, we started with a previously published framework for the calculation of the Gibbs free energy of mixing [121]. For aqueous solutions of a strong electrolyte, the Gibbs free energy of mixing per mole of the system,  $\Delta G_{\text{mix,NT}}$  is defined as:

$$-\frac{\Delta G_{\text{mix,NT}}}{R_g T} = \left[ \sum x_i \ln(\gamma_i x_i) \right]_M - \varphi \left[ \sum x_i \ln(\gamma_i x_i) \right]_{LC} - (1 - \varphi) \left[ \sum x_i \ln(\gamma_i x_i) \right]_{HC} \quad (4)$$

where T is absolute temperature,  $R_g$  is universal gas constant,  $x_i$  is the mole fraction of species i in final mixture, and subscripts M, LC, and HC correspond to mixture, low concentration and high concentration solution respectively. The term  $\varphi$  represents ratio of total moles in LC solution to that in the system, while nonideal behavior of species i as function of the solution composition, pressure, and temperature is accounted for by  $\gamma$ , the activity coefficient. Single electrolyte solutions are defined as consisting of two species, water and dissociated salt ions designated by subscripts w and s, and is represented as,  $\sum x_i \ln(\gamma_i x_i) = x_w \ln(\gamma_w x_w) + x_s \ln(\gamma_s x_s)$ .

Using the equation above, we calculated the  $\Delta G_{\text{mix}}$  for two sets of LC and HC solutions within a 2 g/L gradient of seawater: (1) LC = 33 g/L and HC = 35 g/L, and (2) LC = 35 g/L and HC = 37 g/L. The calculations were performed over a range of  $\varphi$ , a parameter that accounts for relative volumes of LC and HC feed solutions. The results of the calculations are shown in Fig. 23, and the numerical values for the low volume of LC ( $\varphi = 0.1$ ), equal volumes of LC and HC ( $\varphi = 0.5$ ), and excess LC ( $\varphi = 0.9$ ) are provided in Table 6. For both sets of feed salinities, the  $\Delta G_{\text{mix}}$  is maximum when equal volumes of LC and HC ( $\varphi = 0.5$ ) are mixed.

For energy technologies based on salinity-gradients, the efficiency,  $\eta$ , is defined as the fraction of Gibbs free energy of mixing ( $\Delta G_{\text{mix}}$ ) converted to useful work, W ( $\eta = W/\Delta G_{\text{mix}}$ ) [142]. For PRO and RED, the two most advanced salinity-gradient technologies, the estimated  $\eta$  when equal volumes of freshwater and seawater were mixed ( $\varphi = 0.5$ ) is 44% and 18–38%, respectively [121]. The  $\eta$  for other technologies is not available because they are in very early stages of development.

Using the calculated  $\Delta G_{\text{mix}}$  values from Table 6 for  $\varphi = 0.5$  and the estimated fraction of  $\Delta G_{\text{mix}}$  energy converted to useful work reported in the literature of 44% for PRO and 30% for RED, the useful work for the 2 g/L salinity gradient was calculated (Table 7).

The reported energy use in thermal gradient-powered UUVs ranges from 2 to 4 Wh. Based on the useful work in Table 7, the minimum volume and weight of water required to power a UUV using PRO and RED technologies was estimated (Table 8).

The estimated volume of water required to generate the necessary energy to power a UUV is large and not feasible for onboard storage and application for a glider or profiler. However, given that these calculations were based on technologies designed and optimized for seawater-river water mixing and for onshore operation, there may be opportunities for new salinity-gradient technologies designed specifically for powering UUVs. One approach to improving the energy output is adding onboard desalination to increase the available salinity gradient. To investigate the potential for desalination coupled with salinity-gradient energy generation, we calculated the Gibbs free energy of mixing for various salinity combinations with seawater (Fig. 24). In each case, the HC solution is maintained at 0.6 M (seawater) and the concentration of the LC solution is then varied from 1.5 mM (river water) up to 0.594 M. The maximum Gibbs free energy is found in each case, as well as the value of  $\varphi$  that optimizes it. Our results suggest a significant increase in available energy with higher salinity gradients, and these results agree with prior reports about seawater-river water mixing. The increased energy output (up to 10,000x) could bring down the required water volumes to power the UUVs.

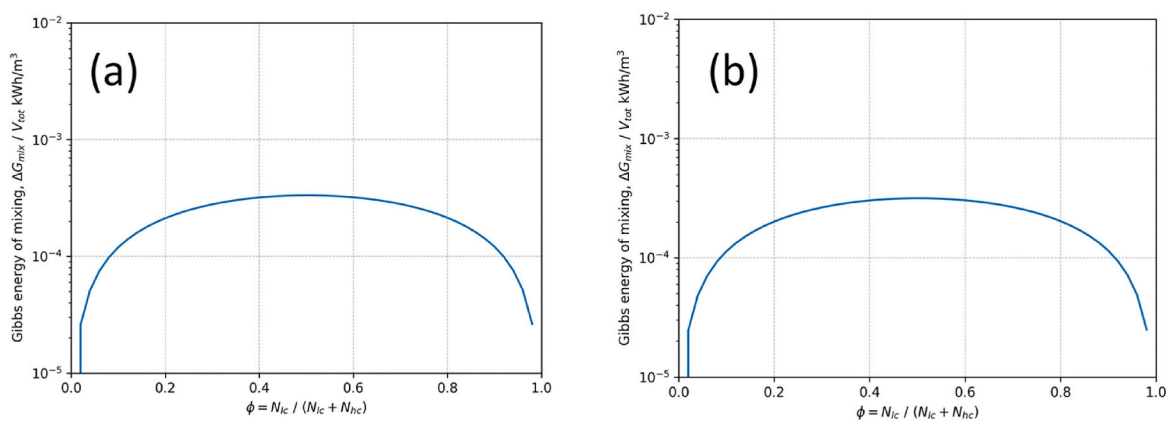


Fig. 23.  $\Delta G_{\text{mix}}$  values as a function of  $\phi$  for (a) LC = 33 g/L and HC = 35 g/L, and (b) LC = 35 g/L and HC = 37 g/L.

Table 6

$\Delta G_{\text{mix}}$  value for low, medium, and high values of  $\phi$ .

$\phi$ ( $N_{\text{LC}}/N_{\text{LC}} + N_{\text{HC}}$ )	$\Delta G_{\text{mix}}$ (kWh/m <sup>3</sup> ) (LC = 33 g/L and HC = 35 g/L)	$\Delta G_{\text{mix}}$ (kWh/m <sup>3</sup> ) (LC = 35 g/L and HC = 37 g/L)
0.1	$1.192 \times 10^{-4}$	$1.131 \times 10^{-4}$
0.5	$3.333 \times 10^{-4}$	$3.159 \times 10^{-4}$
0.9	$1.208 \times 10^{-4}$	$1.144 \times 10^{-4}$

Table 7

Estimated useful work for  $\phi = 0.5$  for salinity gradient of 2 g/L.

Technology	W (kWh/m <sup>3</sup> ) (LC = 33 g/L and HC = 35 g/L)	W (kWh/m <sup>3</sup> ) (LC = 35 g/L and HC = 37 g/L)
PRO	$1.47 \times 10^{-4}$	$1.39 \times 10^{-4}$
RED	$1.0 \times 10^{-4}$	$9.48 \times 10^{-5}$

Table 8

Volume of water required to power a UUV.

Technology	Energy Output Range	Volume Water to Power UUVs (2–4 Wh)	Water Weight to Be Carried ( $\phi = 0.5$ )
PRO	$1 \times 10^{-4}$ Wh/L	20,000–40,000 L	>10,000 kg
	$1.5 \times 10^{-4}$ Wh/L	13,600–27,200 L	>6800 kg
RED	$0.95 \times 10^{-4}$ Wh/L	21,100–42,200 L	>10,550 kg
	$1.4 \times 10^{-4}$ Wh/L	14,300–28,600 L	>7150 kg

### 5. Summary and future outlook

In the last two decades, thermal gradient energy harvesting systems based on PCM for UUVs have been developed and field demonstrated with over 3000 km of mission range for both buoyancy regulation and electrical energy storage. State-of-the-art PCM-based thermal gradient energy systems generated 1.7–2.2 Wh [9,24,32,34,35], which can sufficiently power the Low-power Seaglider (1.5 Wh) or the SOLO II Float (>1.1 Wh) [2,4]. However, those thermal gradient energy harvesting systems based on PCM could not fully power high-energy-demanding UUVs such as the SOCCOM Apex float (5.5 Wh) or PROVOR float (7.3 Wh) [3,13], which incorporate multiple sensors, and the Deep SOLO (7.4 Wh) and Petrel-II Glider (14.7 Wh) [10,12], which require a high-power buoyancy engine for its deep diving operations. In many cases, the buoyancy engine is the most energy hungry component of the float and glider-type UUVs; therefore, reducing the buoyancy engines' energy consumption is key to meeting the energy requirements of UUVs. Development of regenerative electric motors in buoyancy engines is required to reduce their energy consumption. In addition, research effort is required to increase the efficiency of the PCM-based thermal gradient energy systems. Optimization of energy conversion systems for highly efficient conversion from thermal to electric energy is required. Hybrid type (buoyancy regulation and electrical storage) PCM-based energy harvesting systems also will be a possible solution for efficient operation of the UUVs. These hybrid systems use the harvested thermal energy for direct buoyancy change without an electric pump, as well as generating the electrical energy necessary for UUV operation [32]. Volume expansion in the PCM-based UUV is the key to achieve high power output. Comparing to increasing the intrinsic thermal expansion of the PCM molecules, to enhance the thermal conductivity of the appropriate PCMs for UUV applications (C<sub>14</sub>–C<sub>19</sub> alkalines) can facilitate the melting and volume expansion of the material, which will result in an increase for the power generated per profile for a PCM-based UUV. Light weight

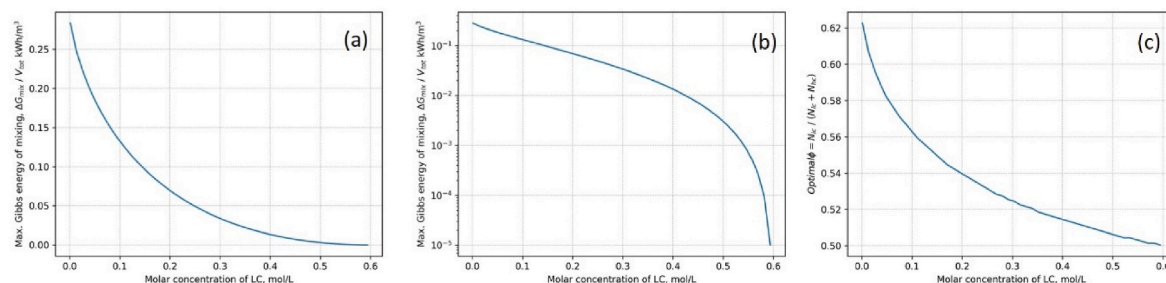


Fig. 24.  $\Delta G_{\text{mix}}$  for HC = 0.6 M (seawater) and LC ranging from 1.5 mM (river water) to 0.59 M (seawater): (a)  $\Delta G_{\text{mix}}$  vs LC, (b)  $\Delta G_{\text{mix}}$  vs LC shown on a logarithmic scale, and (c) optimum  $\phi$  for maximum  $\Delta G_{\text{mix}}$  for the data.

additives with high thermal conductivity that can be well dispersed in the PCM materials are promising to enhance thermal conductivity without adding significant mass and volume to the UUV.

Other emerging technologies such as TEG, SMA, and small-scale thermodynamic cycle systems have potential for use in powering UUVs. However, only limited laboratory tests have been conducted to verify the performance of UUVs that utilize SMA. Thermodynamic cycle-based TEG-based UUVs are only at the early phase of demonstrating component feasibility under controlled conditions and developing system conceptual designs using theoretical calculations and subsea thermal profiles. Simulated results show that 0.05 m<sup>2</sup> of TEGs are needed, while 28.9 kg of PCM are required for generating sufficient energy for UUVs [84]. Further research is needed to improve the thermal-to-hydraulic energy conversion efficiency for PCM-based systems for fully autonomous missions, while system integration and feasibility demonstration in representative field conditions are required for TEG, SMA, and thermodynamic cycle systems to move beyond conceptual design phase.

Our preliminary evaluation suggests that the most advanced salinity-gradient power generation technologies, PRO and RED, are not suitable for powering UUVs. Given that these technologies are designed and optimized for seawater-river water mixing and for onshore operation, there may be opportunities for new salinity-gradient technologies designed specifically for powering UUVs. However, the possibility of new and emerging technologies being viable depends on successful research and development of membranes, electrodes, and system components suitable for operation under harsh marine conditions. Another approach to increasing the power output of salinity-gradient technologies is to increase the available salinity gradient using onboard desalination, but desalination technologies are also plagued with operational inefficiencies and have membrane cost and lifetime issues, so we do not anticipate this to be a viable path forward. Instead, we propose exploring the use of higher salinity gradients in coastal and estuarine regions where seawater mixes with freshwater for distributed coastal monitoring. With recent advancements in sensing technologies and low power data transfer networks, the feasibility of distributed, self-powered sensing systems offers the promise of continuous data acquisition at low cost, particularly in remote coastal areas where grid power or other renewable sources are not available. Salinity gradients are well suited to power such applications, but dedicated research and development of small-scale, microfluidics-based salinity-gradient energy systems are needed.

#### Declaration of competing interest

The authors declare that they have no known competing financial interests or personal relationships that could have appeared to influence the work reported in this paper.

#### Acknowledgments

This research was funded by the U.S. Department of Energy (DOE) Water Power Technologies Office. The study was conducted by Pacific Northwest National Laboratory, which is operated by Battelle for DOE under Contract DEAC05-76RL01830. The views expressed in the article do not necessarily represent the views of the DOE or the U.S. Government. All figures from cited references were reused with permission from the copyright owner. Any further reuse of these figures must first seek additional permissions from the copyright owner.

#### Appendix A. Supplementary data

Supplementary data to this article can be found online at <https://doi.org/10.1016/j.rser.2022.112283>.

#### References

- [1] Cavagnaro RJ, Copping AE, Green R, Greene D, Jenne S, Rose D, et al. Powering the Blue Economy: Progress Exploring Marine Renewable Energy Integration With Ocean Observations. *Mar. Technol. Soc. J.* 2020;54:114–25. <https://doi.org/10.4031/MTSJ.54.6.11>.
- [2] Bruvik EM, Fer I, Våge K, Haugan PM. A revised ocean glider concept to realize Stommel's vision and supplement Argo floats. *Ocean Sci* 2020;16:291–305. <https://doi.org/10.5194/os-16-291-2020>.
- [3] Riser SC, Swift D, Drucker R. Profiling floats in SOCCOM: technical capabilities for studying the southern ocean. *J Geophys Res: Oceans* 2018;123:4055–73. <https://doi.org/10.1002/2017JC013419>.
- [4] King B. Report from the 2nd float and CTD technical workshop. Seattle: University of Washington; 2017.
- [5] NOAA. Hurricane Gliders n.d. <https://www.aoml.noaa.gov/hurricane-glider-project/> (accessed February 22, 2021).
- [6] Argo Program Office. n.d. <https://argo.ucsd.edu/about/> (accessed February 22, 2021).
- [7] Chao Y. Autonomous underwater vehicles and sensors powered by ocean thermal energy. *OCEANS 2016 - Shanghai*; 2016. p. 1–4. <https://doi.org/10.1109/OCEANSAP.2016.7485367>.
- [8] Rudnick DL, Davis RE, Eriksen CC, Fratantoni DM, Perry MJ. Underwater gliders for ocean research. *Mar Technol Soc J* 2004;38:73–84. <https://doi.org/10.4031/002533204787522703>.
- [9] Wang G, Yang Y, Wang S. Ocean thermal energy application technologies for unmanned underwater vehicles: a comprehensive review. *Appl Energy* 2020;278:115752. <https://doi.org/10.1016/j.apenergy.2020.115752>.
- [10] Song Y, Wang Y, Yang S, Wang S, Yang M. Sensitivity analysis and parameter optimization of energy consumption for underwater gliders. *Energy* 2020;191:116506. <https://doi.org/10.1016/j.energy.2019.116506>.
- [11] Gordon L. Recommendations for reports about argo float batteries. University of California San Diego (UCSD); 2017.
- [12] Roemmich D, Sherman JT, Davis RE, Grindley K, McClune M, Parker CJ, et al. Deep SOLO: a full-depth profiling float for the argo program. *J Atmos Ocean Technol* 2019;36. <https://doi.org/10.1175/JTECH-D-19-0066.1>. 1967–81.
- [13] Bittig HC, Maurer TL, Plant JN, Schmechtig C, Wong APS, Claustre H, et al. A BGC-argo guide: planning, deployment, data handling and usage. *Front Mar Sci* 2019;6:502. <https://doi.org/10.3389/fmars.2019.00502>.
- [14] Hockley CJ. Improving seaglider efficiency: an analysis of wing shapes, hull morphologies, and propulsion methods. 2018.
- [15] Woithe HC, Boehm D, Kremer U. Improving Slocum glider dead reckoning using a Doppler velocity log. *OCEANS'11 MTS/IEEE KONA*; 2011. p. 1–5. <https://doi.org/10.23919/OCEANS.2011.6107296>.
- [16] Asakawa K, Watari K, Ohuchi H, Nakamura M, Hyakudome T, Ishihara Y. Buoyancy engine developed for underwater gliders. *Adv Robot* 2016;30:41–9. <https://doi.org/10.1080/01691864.2015.1102647>.
- [17] Zhou H, Fu J, Liu C, Zeng Z, Yu C, Yao B, et al. Dynamic modeling and endurance enhancement analysis of deep-sea gliders with a hybrid buoyancy regulating system. *Ocean Eng* 2020;217:108146. <https://doi.org/10.1016/j.oceaneng.2020.108146>.
- [18] Yang Y, Wang Y, Ma Z, Wang S. A thermal engine for underwater glider driven by ocean thermal energy. *Appl Therm Eng* 2016;99:455–64. <https://doi.org/10.1016/j.applthermaleng.2016.01.038>.
- [19] Simonetti PJ. Low cost endurance ocean profiler. *Sea Technol* 1998:17–21.
- [20] Webb DC, Simonetti PJ, Jones CP. SLOCUM: an underwater glider propelled by environmental energy. *IEEE J Ocean Eng* 2001;26:447–52. <https://doi.org/10.1109/48.972077>.
- [21] Lippsett L. Green' energy powers undersea glider. *Woods Hole Oceanographic Institution*; 2008.
- [22] Webb Research Corporation. 2004. [https://web.archive.org/web/20081031132213/www.webbresearch.com/thermal\\_glider.htm](https://web.archive.org/web/20081031132213/www.webbresearch.com/thermal_glider.htm) (accessed February 22, 2021).
- [23] Zhang H-W, Wang Y-H, Lian Z-G. Application and improvement of the interlayer thermal engine powered by ocean thermal energy in an underwater glider. In: 2009 asia-pacific power and energy engineering conference; 2009. p. 1–4. <https://doi.org/10.1109/APPEEC.2009.4918179>.
- [24] Wang G, Yang Y, Wang S, Zhang H, Wang Y. Efficiency analysis and experimental validation of the ocean thermal energy conversion with phase change material for underwater vehicle. *Appl Energy* 2019;248:475–88. <https://doi.org/10.1016/j.apenergy.2019.04.146>.
- [25] Kuznik F, Johannes K, David D. 13 - integrating phase change materials (PCMs) in thermal energy storage systems for buildings. In: Cabeza LF, editor. *Advances in thermal energy storage systems*. Woodhead Publishing; 2015. p. 325–53. <https://doi.org/10.1533/9781782420965.2.325>.
- [26] Shamberger PJ, Bruno NM. Review of metallic phase change materials for high heat flux transient thermal management applications. *Appl Energy* 2020;258:113955. <https://doi.org/10.1016/j.apenergy.2019.113955>.
- [27] Pilon L, Benjamin Y, Alexander T, Amanda F, Gaurav S. Thermophysical properties of phase change materials n.d. <http://www.seas.ucla.edu/~pilon/downloads.htm#section4> (accessed February 22, 2021).
- [28] Hari Krishnan S, Deenadhayalan M, Kalaiselvam S. Experimental investigation of solidification and melting characteristics of composite PCMs for building heating application. *Energy Convers Manag* 2014;86:864–72. <https://doi.org/10.1016/j.enconman.2014.06.042>.
- [29] Williams AS. Design of a low-cost open-source underwater glider. 2018. <https://engrxiv.org/kvqmh/>. [Accessed 22 February 2021]. accessed.

- [30] Wang G, Ha DS, Wang KG. Harvesting environmental thermal energy using solid/liquid phase change materials. *J Intell Mater Syst Struct* 2018;29:1632–48. <https://doi.org/10.1177/1045389X17742733>.
- [31] Aesar, A. (A14834) 2021. <https://www.chemicalbook.com/Price/Dodecane.htm> (accessed February 22, 2021).
- [32] Haldeman CD, Schofield O, Webb DC, Valdez TI, Jones JA. Implementation of energy harvesting system for powering thermal gliders for long duration ocean research. *OCEANS 2015 - MTS/IEEE Washington*; 2015. p. 1–5. <https://doi.org/10.23919/OCEANS.2015.7404559>.
- [33] Kim H, Choi J-Y, Park J, Ruda M, Prasad R, Chao Y, et al. Towards the optimal operation of a thermal-recharging float in the ocean. *Ocean Eng* 2018;156: 381–95. <https://doi.org/10.1016/j.oceaneng.2018.02.043>.
- [34] Bin Z, Meng W, Huajiang L, Ge W. Research on the ocean thermal power generation technology for small-sized Marine Observation Vehicles. *J Ocean Technol* 2015;34:78–82.
- [35] Shepard P. Seatrec Secures Seed Financing for Ocean Energy Harvesting Tech n.d. <https://eepower.com/news/seatrec-secures-seed-financing-for-ocean-energy-harvesting-tech/#> (accessed February 22, 2021).
- [36] Valdez TI, Jones AJ, Leland RS. Self-powered underwater robot for ocean exploration and beyond. 2011. <https://trs.jpl.nasa.gov/handle/2014/43561>. [Accessed 22 February 2021]. accessed.
- [37] Navis-SL1. SL1-powered profiling float n.d. <https://seatrec.com/wp-content/uploads/2020/08/SEATREC-DATA-SHEET-NAVIS-SL1-061720.pdf> (accessed February 22, 2021).
- [38] Glenn S. <https://marine.rutgers.edu/cool/data/gliders/configure/?type=notes&did=383>. [Accessed 17 February 2022]. accessed.
- [39] Vélez C, Khayet M, Zárate JMO de. Temperature-dependent thermal properties of solid/liquid phase change even-numbered n-alkanes: n-Hexadecane, n-octadecane and n-eicosane. *Appl Energy* 2015;143:383–94. <https://doi.org/10.1016/j.apenergy.2015.01.054>.
- [40] Hamed A-S, Sadeghzadeh S. Conceptual design of a 5 MW OTEC power plant in the Oman Sea. *J Marine Eng Technol* 2017;16:94–102. <https://doi.org/10.1080/20464177.2017.1320839>.
- [41] Mondieig D, Rajabalee F, Metivaud V, Oonk HAJ, Cuevas-Diarte MA. n-Alkane binary molecular alloys. *Chem Mater* 2004;16:786–98. <https://doi.org/10.1021/cm031169p>.
- [42] Vélez C, Zárate JMO de, Khayet M. Thermal properties of n-pentadecane, n-heptadecane and n-nonadecane in the solid/liquid phase change region. *Int J Therm Sci* 2015;94:139–46. <https://doi.org/10.1016/j.ijthermalsci.2015.03.001>.
- [43] Himran S, Suwono A, Mansoori GA. Characterization of alkanes and paraffin waxes for application as phase change energy storage medium. *Energy Sources* 1994;16:117–28. <https://doi.org/10.1080/00908319408909065>.
- [44] Domalski ES, Hearing ED. Heat capacities and entropies of organic compounds in the condensed phase. Volume III. *J Phys Chem Ref Data* 1996;25:1–525. <https://doi.org/10.1063/1.555985>.
- [45] Fan L, Khodadadi JM. Thermal conductivity enhancement of phase change materials for thermal energy storage: a review. *Renew Sustain Energy Rev* 2011; 15:24–46. <https://doi.org/10.1016/j.rser.2010.08.007>.
- [46] Wu S, Yan T, Kuai Z, Pan W. Thermal conductivity enhancement on phase change materials for thermal energy storage: a review. *Energy Storage Mater* 2020;25: 251–95. <https://doi.org/10.1016/j.ensm.2019.10.010>.
- [47] Dhaidan NS, Khodadadi JM. Improved performance of latent heat energy storage systems utilizing high thermal conductivity fins: a review. *J Renew Sustain Energy* 2017;9:034103. <https://doi.org/10.1063/1.4989738>.
- [48] Wu MQ, Wu S, Cai YF, Wang RZ, Li TX. Form-stable phase change composites: preparation, performance, and applications for thermal energy conversion, storage and management. *Energy Storage Mater* 2021;42:380–417. <https://doi.org/10.1016/j.ensm.2021.07.019>.
- [49] Wu S, Li T, Tong Z, Chao J, Zhai T, Xu J, et al. High-performance thermally conductive phase change composites enabled by large-size oriented graphite sheets for scalable thermal energy harvesting. *Adv Mater* 2019;31:1905099. <https://doi.org/10.1002/adma.201905099>.
- [50] Li T, Wu M, Wu S, Xiang S, Xu J, Chao J, et al. Highly conductive phase change composites enabled by vertically-aligned reticulated graphite nanoplatelets for high-temperature solar photo/electro-thermal energy conversion, harvesting and storage. *Nano Energy* 2021;89:106338. <https://doi.org/10.1016/j.nanoen.2021.106338>.
- [51] Wu M, Li T, Wang P, Wu S, Wang R, Lin J. Dual-encapsulated highly conductive and liquid-free phase change composites enabled by polyurethane/graphite nanoplatelets hybrid networks for efficient energy storage and thermal management. *Small* 2021. <https://doi.org/10.1002/sml.202105647>. n/a: 2105647.
- [52] Wu S, Li TX, Wu MQ, Xu JX, Hu YH, Chao JW, et al. Highly thermally conductive and flexible phase change composites enabled by polymer/graphite nanoplatelet-based dual networks for efficient thermal management. *J Mater Chem* 2020;3: 20011–20. <https://doi.org/10.1039/D0TA05904H>.
- [53] Li TX, Wu DL, He F, Wang RZ. Experimental investigation on copper foam/hydrated salt composite phase change material for thermal energy storage. *Int J Heat Mass Tran* 2017;115:148–57. <https://doi.org/10.1016/j.ijheatmasstransfer.2017.07.056>.
- [54] Atinafu DG, Dong W, Huang X, Gao H, Wang G. Introduction of organic-organic eutectic PCM in mesoporous N-doped carbons for enhanced thermal conductivity and energy storage capacity. *Appl Energy* 2018;211:1203–15. <https://doi.org/10.1016/j.apenergy.2017.12.025>.
- [55] Mehrali M, Latibari ST, Mehrali M, Mahlia TMI, Sadeghinezhad E, Metselaar HSC. Preparation of nitrogen-doped graphene/palmitic acid shape stabilized composite phase change material with remarkable thermal properties for thermal energy storage. *Appl Energy* 2014;135:339–49. <https://doi.org/10.1016/j.apenergy.2014.08.100>.
- [56] Chen X, Gao H, Xing L, Dong W, Li A, Cheng P, et al. Nanoconfinement effects of N-doped hierarchical carbon on thermal behaviors of organic phase change materials. *Energy Storage Mater* 2019;18:280–8. <https://doi.org/10.1016/j.ensm.2018.08.024>.
- [57] Wang J, Jia X, Atinafu DG, Wang M, Wang G, Lu Y. Synthesis of “graphenelike” mesoporous carbons for shape-stabilized phase change materials with high loading capacity and improved latent heat. *J Mater Chem* 2017;5:24321–8.
- [58] Wang J, Huang X, Gao H, Li A, Wang C. Construction of CNT@Cr-MIL-101-NH2 hybrid composite for shape-stabilized phase change materials with enhanced thermal conductivity. *Chem Eng J* 2018;350:164–72. <https://doi.org/10.1016/j.cej.2018.05.190>.
- [59] Sami S, Etesami N. Improving thermal characteristics and stability of phase change material containing TiO2 nanoparticles after thermal cycles for energy storage. *Appl Therm Eng* 2017;124:346–52. <https://doi.org/10.1016/j.applthermaleng.2017.06.023>.
- [60] Warzoha RJ, Fleischer AS. Effect of carbon nanotube interfacial geometry on thermal transport in solid-liquid phase change materials. *Appl Energy* 2015;154: 271–6. <https://doi.org/10.1016/j.apenergy.2015.04.121>.
- [61] Mohamed NH, Soliman FS, Maghraby HE, Moustafa YM. Thermal conductivity enhancement of treated petroleum waxes, as phase change material, by  $\alpha$  nano alumina: energy storage. *Renew Sustain Energy Rev* 2017;70:1052–8. <https://doi.org/10.1016/j.rser.2016.12.009>.
- [62] Su D, Jia Y, Alva G, Tang F, Fang G. Preparation and thermal properties of n-octadecane/stearic acid eutectic mixtures with hexagonal boron nitride as phase change materials for thermal energy storage. *Energy Build* 2016;131: 35–41. <https://doi.org/10.1016/j.enbuild.2016.09.022>.
- [63] Yuan W, Yang X, Zhang G, Li X. A thermal conductive composite phase change material with enhanced volume resistivity by introducing silicon carbide for battery thermal management. *Appl Therm Eng* 2018;144:551–7. <https://doi.org/10.1016/j.applthermaleng.2018.07.095>.
- [64] Chiu JN. Heat transfer aspects of using phase change material in thermal energy storage applications. *KTH Royal Institute of Technology*; 2011.
- [65] Chibani A, Merouani S. Acceleration of heat transfer and melting rate of a phase change material by nanoparticles addition at low concentrations. *Int J Thermophys* 2021;42:66. <https://doi.org/10.1007/s10765-021-02822-z>.
- [66] Li T, Lee J-H, Wang R, Kang YT. Enhancement of heat transfer for thermal energy storage application using stearic acid nanocomposite with multi-walled carbon nanotubes. *Energy* 2013;55:752–61. <https://doi.org/10.1016/j.energy.2013.04.010>.
- [67] Narain J. Thermal buoyancy engine. 2014. <https://jnarain.mit.edu/thermal-buoyancy-engine>. [Accessed 22 February 2021]. accessed.
- [68] Angilella AJ, Gandhi FS, Miller TF. Design and testing of a shape memory alloy buoyancy engine for unmanned underwater vehicles. *Smart Mater Struct* 2015; 24:115018. <https://doi.org/10.1088/0964-1726/24/11/115018>.
- [69] Angilella AJ, Gandhi FS, Miller TF. Simulating a shape memory alloy buoyancy heat engine for undersea gliders. *OCEANS 2015 - MTS/IEEE Washington*; 2015. p. 1–10. <https://doi.org/10.23919/OCEANS.2015.7404537>.
- [70] Barbarino S, Flores EIS, Ajaj RM, Dayyani I, Friswell MI. A review on shape memory alloys with applications to morphing aircraft. *Smart Mater Struct* 2014; 23:063001. <https://doi.org/10.1088/0964-1726/23/6/063001>.
- [71] Nippon Steel. Shape-memory alloys n.d. <https://www.nipponsteel.com/en/product/railway-automotive-machinery-parts/list/19.html> (accessed February 22, 2021).
- [72] ATI NiTi Alloys. n.d. <https://www.atimetals.com/Products/Pages/niti.aspx> (accessed February 22, 2021).
- [73] Jani JM, Leary M, Subic A, Gibson MA. A review of shape memory alloy research, applications and opportunities. *Mater Des* 2014;56:1078–113. <https://doi.org/10.1016/j.matdes.2013.11.084>.
- [74] Copper Development Association Inc. Shape Memory and Superelastic Alloys n.d. <https://www.copper.org/publications/newsletters/innovations/1999/07/shape.html> (accessed February 7, 2022).
- [75] Reade International Corp. Shape Memory Alloys and Wires (SMA) n.d. <https://www.reade.com/products/shape-memory-alloys-and-wires-sma> (accessed February 7, 2022).
- [76] Pulidindi K, Mukherjee S. Shape Memory Alloys Market Size By Product (NiTi, Copper Based, Others), By End-User (Biomedical, Aerospace & Defense, Automotive, Household Appliances, Others), Industry Analysis Report, Regional Outlook, Application Growth Potential, Price Trends, Competitive Market Share & Forecast, 2019 – 2025 n.d. <https://www.gminsights.com/industry-analysis/shape-memory-alloys-market> (accessed February 7, 2022).
- [77] Global Market Insights, Inc. Shape Memory Alloys Market Share to Hit \$20 Bn by 2025: Global Market Insights, Inc n.d. <https://www.prnewswire.com/news-releases/shape-memory-alloys-market-share-to-hit-20-bn-by-2025-global-market-insights-inc-300841050.html> (accessed February 7, 2022).
- [78] Shape Memory Alloy Market – Forecast (2021-2026). n.d. <https://www.industryarc.com/Report/16235/shape-memory-alloy-market.html> (accessed February 22, 2021).
- [79] Yang C, Abanteriba S, Becker A. A review of shape memory alloy based filtration devices. *AIP Adv* 2020;10:060701. <https://doi.org/10.1063/1.5133981>.
- [80] Johnson Matthey Inc.. Nitinol technical properties. <https://matthey.com/en/pr-oducts-and-services/medical-components/resource-library/nitinol-technical-properties>. [Accessed 22 February 2021]. accessed.

- [81] Nexmetal corporation. n.d. [https://nexmetal.com/products/nitinol-memory-wire?gclid=CjwKCAiAudD\\_BRBxEiwAudaKX0JlmR4ViY3pXJNZYUuaP4k3mw7hEV1SzCdqhHE9kA8DgP0M3MldBoC9BgQAvD.BwE&variant=32218742587434](https://nexmetal.com/products/nitinol-memory-wire?gclid=CjwKCAiAudD_BRBxEiwAudaKX0JlmR4ViY3pXJNZYUuaP4k3mw7hEV1SzCdqhHE9kA8DgP0M3MldBoC9BgQAvD.BwE&variant=32218742587434) (accessed February 22, 2021).
- [82] Orr B, Akbarzadeh A, Mochizuki M, Singh R. A review of car waste heat recovery systems utilising thermoelectric generators and heat pipes. *Appl Therm Eng* 2016; 101:490–5. <https://doi.org/10.1016/j.applthermaleng.2015.10.081>.
- [83] Hewawasam LS, Jayasena AS, Anfan MMM, Ranasinghe RACP, Wijewardane MA. Waste heat recovery from thermo-electric generators (TEGs). *Energy Rep* 2020;6: 474–9. <https://doi.org/10.1016/j.egy.2019.11.105>.
- [84] Carneiro JF, Almeida FG de. Model and simulation of the energy retrieved by thermoelectric generators in an underwater glider. *Energy Convers Manag* 2018; 163:38–49. <https://doi.org/10.1016/j.enconman.2018.02.031>.
- [85] Dewan A, Ay SU, Karim MN, Beyenal H. Alternative power sources for remote sensors: a review. *J Power Sources* 2014;245:129–43. <https://doi.org/10.1016/j.jpowsour.2013.06.081>.
- [86] Selvan KV, Hasan MN, Mohamed Ali MS. State-of-the-Art reviews and analyses of emerging research findings and achievements of thermoelectric materials over the past years. *J Electron Mater* 2019;48:745–77. <https://doi.org/10.1007/s11664-018-06838-4>.
- [87] Wang P, Li JE, Wang BL, Shimada T, Hirakata H, Zhang C. Lifetime prediction of thermoelectric devices under thermal cycling. *J Power Sources* 2019;437:226861. <https://doi.org/10.1016/j.jpowsour.2019.226861>.
- [88] EVERREDtronics 2009. <http://www.everredtronics.com/Thermal.html>. [Accessed 22 February 2021]. accessed.
- [89] Atouei SA, Rezanian A, Ranjbar AA, Rosendahl LA. Protection and thermal management of thermoelectric generator system using phase change materials: an experimental investigation. *Energy* 2018;156:311–8. <https://doi.org/10.1016/j.energy.2018.05.109>.
- [90] Sault B. Scientific guide to understanding thermoelectric generators and TEG products for converting heat to TEG power. 2018. <https://www.tegmart.com/info/guide-to-understanding-and-using-teg-power-and-products/>. [Accessed 22 February 2021]. accessed.
- [91] TECTEG (TEG1-1263-4.3). n.d. <https://thermoelectric-generator.com/product/teg1-1263-4-3/> (accessed February 22, 2021).
- [92] Yuan H, Mei N, Hu S, Wang L, Yang S. Experimental investigation on an ammonia-water based ocean thermal energy conversion system. *Appl Therm Eng* 2013;61:327–33. <https://doi.org/10.1016/j.applthermaleng.2013.07.050>.
- [93] Faizal M, Ahmed MR. Experimental studies on a closed cycle demonstration OTEC plant working on small temperature difference. *Renew Energy* 2013;51:234–40. <https://doi.org/10.1016/j.renene.2012.09.041>.
- [94] Howard R. Underwater vehicle. 2011. <https://patentimages.storage.googleapis.com/60/2d/26/80d03b03558c39/US8065972.pdf>. [Accessed 8 February 2022]. accessed.
- [95] Yoon J-I, Seol S-H, Son C-H, Jung S-H, Kim Y-B, Lee H-S, et al. Analysis of the high-efficiency EP-OTEC cycle using R152a. *Renew Energy* 2017;105:366–73. <https://doi.org/10.1016/j.renene.2016.12.019>.
- [96] Wang H, Xu J, Yang X, Miao Z, Yu C. Organic Rankine cycle saves energy and reduces gas emissions for cement production. *Energy* 2015;86:59–73. <https://doi.org/10.1016/j.energy.2015.03.112>.
- [97] OTEC beats warming. Ost effective OTEC (ocean thermal energy conversion) electrical power plant. n.d. <https://www.climatecolab.org/contests/2015/harnessing-the-power-of-mit-alumni/c/proposal/1325332>. [Accessed 7 February 2022]. accessed.
- [98] Kongtragool B, Wongwiset S. A review of solar-powered Stirling engines and low temperature differential Stirling engines. *Renew Sustain Energy Rev* 2003;7: 131–54. [https://doi.org/10.1016/S1364-0321\(02\)00053-9](https://doi.org/10.1016/S1364-0321(02)00053-9).
- [99] Martaj N, Grosu L, Rochelle P. Thermodynamic study of a low temperature difference stirling engine at steady state operation. *Int J Therm* 2007;10:165–76.
- [100] Jokar H, Tavakolpour-Saleh AR. A novel solar-powered active low temperature differential Stirling pump. *Renew Energy* 2015;81:319–37. <https://doi.org/10.1016/j.renene.2015.03.041>.
- [101] Boutammache N, Knorr J. Field-test of a solar low delta-T Stirling engine. *Sol Energy* 2012;86:1849–56. <https://doi.org/10.1016/j.solener.2012.03.001>.
- [102] Iwamoto F, Toda F, Hirata K, Takeuchi M, Yamamoto T. Comparison of low- and high temperature differential stirling engines. 1997. p. 29–38.
- [103] Kaushik SC, Kumar S. Finite time thermodynamic analysis of endoreversible Stirling heat engine with regenerative losses. *Energy* 2000;25:989–1003. [https://doi.org/10.1016/S0360-5442\(00\)00023-2](https://doi.org/10.1016/S0360-5442(00)00023-2).
- [104] Cloud M. What is the energy density of a lithium-ion battery?. 2020. <https://www.fluxpower.com/blog/what-is-the-energy-density-of-a-lithium-ion-battery>. [Accessed 27 September 2021]. accessed.
- [105] Wang M, Jing R, Zhang H, Meng C, Li N, Zhao Y. An innovative Organic Rankine Cycle (ORC) based Ocean Thermal Energy Conversion (OTEC) system with performance simulation and multi-objective optimization. *Appl Therm Eng* 2018; 145:743–54. <https://doi.org/10.1016/j.applthermaleng.2018.09.075>.
- [106] Banichik LD, Sharqawy MH, Lienhard JH. Limits of power production due to finite membrane area in pressure retarded osmosis. *J Membr Sci* 2014;468:81–9. <https://doi.org/10.1016/j.memsci.2014.05.021>.
- [107] Han G, Zhang S, Li X, Chung T-S. High performance thin film composite pressure retarded osmosis (PRO) membranes for renewable salinity-gradient energy generation. *J Membr Sci* 2013;440:108–21. <https://doi.org/10.1016/j.memsci.2013.04.001>.
- [108] Ingole PG, Kim KH, Park CH, Choi WK, Lee HK. Preparation, modification and characterization of polymeric hollow fiber membranes for pressure-retarded osmosis. *RSC Adv* 2014;4:51430–9. <https://doi.org/10.1039/C4RA07619B>.
- [109] Tawalbeh M, Al-Orthman A, Abdelwahab N, Alami AH, Olabi AG. Recent developments in pressure retarded osmosis for desalination and power generation. *Renew Sustain Energy Rev* 2021;138:110492. <https://doi.org/10.1016/j.rser.2020.110492>.
- [110] Helfer F, Lemckert C, Anissimov YG. Osmotic power with pressure retarded osmosis: theory, performance and trends – a review. *J Membr Sci* 2014;453: 337–58. <https://doi.org/10.1016/j.memsci.2013.10.053>.
- [111] Lee C, Chae SH, Yang E, Kim S, Kim JH, Kim IS. A comprehensive review of the feasibility of pressure retarded osmosis: recent technological advances and industrial efforts towards commercialization. *Desalination* 2020;491:114501. <https://doi.org/10.1016/j.desal.2020.114501>.
- [112] Achilli A, Childress AE. Pressure retarded osmosis: From the vision of Sidney Loeb to the first prototype installation — Review. *Desalination* 2010;261:205–11. <https://doi.org/10.1016/j.desal.2010.06.017>.
- [113] Lee S, Choi J, Park Y-G, Shon H, Ahn CH, Kim S-H. Hybrid desalination processes for beneficial use of reverse osmosis brine: current status and future prospects. *Desalination* 2019;454:104–11. <https://doi.org/10.1016/j.desal.2018.02.002>.
- [114] Tufa RA, Pawlowski S, Veerman J, Bouzek K, Fontananova E, Profio G di, et al. Progress and prospects in reverse electro dialysis for salinity gradient energy conversion and storage. *Appl Energy* 2018;225:290–331. <https://doi.org/10.1016/j.apenergy.2018.04.111>.
- [115] Daniilidis A, Vermaas DA, Herber R, Nijmeijer K. Experimentally obtainable energy from mixing river water, seawater or brines with reverse electro dialysis. *Renew Energy* 2014;64:123–31. <https://doi.org/10.1016/j.renene.2013.11.001>.
- [116] Tufa RA, Curcio E, Brauns E, Baak W van, Fontananova E, Profio GD. Membrane distillation and reverse electro dialysis for near-zero liquid discharge and low energy seawater desalination. *J Membr Sci* 2015;496:325–33. <https://doi.org/10.1016/j.memsci.2015.09.008>.
- [117] Zhu X, He W, Logan BE. Reducing pumping energy by using different flow rates of high and low concentration solutions in reverse electro dialysis cells. *J Membr Sci* 2015;486:215–21. <https://doi.org/10.1016/j.memsci.2015.03.035>.
- [118] Desalination. RED-Powered Power Pilot to Start Trials in February n.d. <https://www.desalination.biz/desalination/red-powered-power-pilot-to-start-trials-in-february/> (accessed February 7, 2022).
- [119] Kim Y, Logan BE. Microbial reverse electro dialysis cells for synergistically enhanced power production. *Environ Sci Technol* 2011;45:5834–9. <https://doi.org/10.1021/es200979b>.
- [120] Brogioli D, Mantia FL. Chapter 5 - capacitive energy extraction from double layer expansion (CDLE). Fundamentals of the method. In: Ahualli S, Delgado AV, editors. Charge and energy storage in electrical double layers, vol. 24. Elsevier; 2018. p. 87–117. <https://doi.org/10.1016/B978-0-12-811370-7.00005-X>.
- [121] Yip NY, Brogioli D, Hamelers HVM, Nijmeijer K. Salinity gradients for sustainable energy: primer, progress, and prospects. *Environ Sci Technol* 2016;50:12072–94. <https://doi.org/10.1021/acs.est.6b03448>.
- [122] Yu J, Ma T. Harvesting blue energy with carbon electrodes of asymmetric nanopore distributions. *Nano Energy* 2021;82:105766. <https://doi.org/10.1016/j.nanoen.2021.105766>.
- [123] Hatzell MC, Cusick RD, Logan BE. Capacitive mixing power production from salinity gradient energy enhanced through exoelectrogen-generated ionic currents. *Energy Environ Sci* 2014;7:1159–65. <https://doi.org/10.1039/C3EE43823F>.
- [124] Lee J, Yoon H, Lee J, Kim T, Yoon J. Extraction of salinity-gradient energy by a hybrid capacitive-mixing system. *ChemSusChem* 2017;10:1600–6. <https://doi.org/10.1002/cssc.201601656>.
- [125] Rica RA, Ziano R, Salerno D, Mantegazza F, Van Roij R, Brogioli D. Capacitive mixing for harvesting the free energy of solutions at different concentrations. *Entropy* 2013;15:1388–407. <https://doi.org/10.3390/e15041388>.
- [126] Siekierka A, Smolińska-Kempisty K, Bryjak M. Charge-doped electrodes for power production using the salinity gradient in CapMix. *Desalination* 2020;495:114670. <https://doi.org/10.1016/j.desal.2020.114670>.
- [127] Tan G, Zhu X. Polyelectrolyte-coated copper hexacyanoferrate and bismuth oxychloride electrodes for efficient salinity gradient energy recovery in capacitive mixing. *Energy Technol* 2020;8:1900863. <https://doi.org/10.1002/ente.201900863>.
- [128] Zhan F, Wang G, Wu T, Dong Q, Meng Y, Wang J, et al. High performance asymmetric capacitive mixing with oppositely charged carbon electrodes for energy production from salinity differences. *J Mater Chem* 2017;5:20374–80.
- [129] Final Report Summary, CAPMIX, European Commission n.d. <https://cordis.europa.eu/project/id/256868/reporting> (accessed January 20, 2021).
- [130] Hidayat S, Song Y-H, Park J-Y. A comparison of mono- and multi-valent ions as stack feed solutions in microbial reverse-electro dialysis cells and their effects on hydrogen generation. *Int Biodeterior Biodegrad* 2016;113:28–33. <https://doi.org/10.1016/j.ibiod.2016.03.008>.
- [131] Cusick RD, Kim Y, Logan BE. Energy capture from thermolytic solutions in microbial reverse-electro dialysis cells. *Science* 2012;335:1474–7. <https://doi.org/10.1126/science.1219330>.
- [132] Zhu X, Hatzell MC, Logan BE. Microbial reverse-electro dialysis electrolysis and chemical-production cell for H<sub>2</sub> production and CO<sub>2</sub> sequestration. *Environ Sci Technol Lett* 2014;1:231–5. <https://doi.org/10.1021/ez500073q>.
- [133] Mei Y, Tang CY. Recent developments and future perspectives of reverse electro dialysis technology: a review. *Desalination* 2018;425:156–74. <https://doi.org/10.1016/j.desal.2017.10.021>.
- [134] Effendi AJ, Hidayat S, Syafrudin, Ramadan BS, Purnawan C, Park J-Y. Performance of microbial reverse-electro dialysis cells for power generation at different external resistance. *Air Soil Water Res* 2020;13. <https://doi.org/10.1177/1178622120960086>.

- [135] Kim Y, Logan BE. Hydrogen production from inexhaustible supplies of fresh and salt water using microbial reverse-electrodialysis electrolysis cells. *Proc Natl Acad Sci Unit States Am* 2011;108:16176–81. <https://doi.org/10.1073/pnas.1106335108>.
- [136] Zhu X, Yang W, Hatzell MC, Logan BE. Energy recovery from solutions with different salinities based on swelling and shrinking of hydrogels. *Environ Sci Technol* 2014;48:7157–63. <https://doi.org/10.1021/es500909q>.
- [137] Bui TQ, Cao VD, Do NBD, Christoffersen TE, Wang W, Kjøniksen A-L. Salinity gradient energy from expansion and contraction of poly(allylamine hydrochloride) hydrogels. *ACS Appl Mater Interfaces* 2018;10:22218–25. <https://doi.org/10.1021/acsami.8b05333>.
- [138] Arens L, Weibenfeld F, Klein CO, Schlag K, Wilhelm M. Osmotic engine: translating osmotic pressure into macroscopic mechanical force via poly(acrylic acid) based hydrogels. *Adv Sci* 2017;4:1700112. <https://doi.org/10.1002/advs.201700112>.
- [139] Zavahir S, Krupa I, AlMaadeed SA, Tkac J, Kasak P. Polyzwitterionic hydrogels in engines based on the antipolyelectrolyte effect and driven by the salinity gradient. *Environ Sci Technol* 2019;53:9260–8. <https://doi.org/10.1021/acs.est.8b06377>.
- [140] Bui TQ, Cao VD, Wang W, Kjøniksen A-L. Recovered energy from salinity gradients utilizing various poly(acrylic acid)-based hydrogels. *Polymers* 2021;13. <https://doi.org/10.3390/polym13040645>.
- [141] Bui TQ, Cao VD, Wang W, Nguyen TH, Kjøniksen A-L. Energy lost in a hydrogel osmotic engine due to a pressure drop. *Ind Eng Chem Res* 2021;60:13348–57. <https://doi.org/10.1021/acs.iecr.1c00409>.
- [142] Yip NY, Elimelech M. Comparison of energy efficiency and power density in pressure retarded osmosis and reverse electro dialysis. *Environ Sci Technol* 2014; 48:11002–12. <https://doi.org/10.1021/es5029316>.
- [143] Long R, Kuang Z, Liu Z, Liu W. Reverse electro dialysis in bilayer nanochannels: salinity gradient-driven power generation. *Phys Chem Chem Phys* 2018;20: 7295–302. <https://doi.org/10.1039/C7CP08394G>.
- [144] Salinity gradient energy: technology. <https://www.irena.org/publications/2014/Jun/Salinity-gradient#:~:text=Salinity%20gradient%20power%20is%20the,river%20flows%20into%20the%20sea.&text=Successive%20technology%20briefs%20have%20highlighted%20a%20wide%20range%20of%20renewable%20energy%20solutions>. [Accessed 20 January 2021].
- [145] Papapetrou M, Kumpavat K. 10 - environmental aspects and economics of salinity gradient power (SGP) processes. In: Cipollina A, Micale G, editors. *Sustainable energy from salinity gradients*. Woodhead Publishing; 2016. p. 315–35. <https://doi.org/10.1016/B978-0-08-100312-1.00010-9>.
- [146] Han G, Zhou J, Wan C, Yang T, Chung T-S. Investigations of inorganic and organic fouling behaviors, antifouling and cleaning strategies for pressure retarded osmosis (PRO) membrane using seawater desalination brine and wastewater. *Water Res* 2016;103:264–75. <https://doi.org/10.1016/j.watres.2016.07.040>.
- [147] Cheng ZL, Li X, Chung T-S. The forward osmosis-pressure retarded osmosis (FO-PRO) hybrid system: a new process to mitigate membrane fouling for sustainable osmotic power generation. *J Membr Sci* 2018;559:63–74. <https://doi.org/10.1016/j.memsci.2018.04.036>.